Nondimensional Framework for a Hall Thruster Discharge and Facility Effects

IEPC-2025-201

Presented at the 39th International Electric Propulsion Conference

Imperial College London • London, United Kingdom

14-19 September 2025

Julian Lopez-Uricoechea[1], Naia Butler-Craig[2], Dan Lev[3], Mitchell L. R. Walker[4],
Georgia Institute of Technology, Atlanta, GA, 30332, U.S.A

Abstract: This work presents a robust nondimensionalization of the Hall effect thruster discharge and its facility effects. We define 23 nondimensional discharge parameters and five nondimensional facility effect parameters that are independent and are intended to capture all the relevant physics of the discharge and facility effects for atomic propellants. From the nondimensional discharge parameters, we find that exact similarity is only possible between thrusters if wall effects are negligible. We also define novel approximate similarity laws based on three nondimensional parameters in addition to geometric similarity that can cover a larger range of discharge powers and operation on different propellants. The similarity laws for different propellants suggest that HETs may not need to be redesigned to operate at similar operating conditions between different propellants. We then develop a nondimensional framework to analyze existing studies of vacuum facilities that combines the nondimensional facility parameters with the nondimensional discharge parameters and defines five new nondimensional facility effect parameters. We use this framework to reduce the dimensionality of existing data of thrust as a function of facility background pressure at different discharge conditions. Specifically, at low background pressures, the normalized thrust as a function of certain nondimensional facility effects is within measurement uncertainty between discharge conditions that differ by either anode mass flow rate, discharge voltage, or cathode flow fraction. This nondimensional framework could be used to design experiments to find a correction for thrust at a given background pressure that can be applied to a wide range of discharge conditions.

I. Introduction

Hall effect thrusters (HETs) have significant flight heritage, but the underlying physics of their operation is poorly understood, such that there is no fully predictive model of HET performance and lifetime. As a result, HET designs have evolved through decades of incremental improvement through experiments to achieve their current level of performance. However, this reliance on experiments has led to two active problems in HET development. First, HETs

[1] Graduate Research Assistant, School of Aerospace Engineering, jlopezur3@gatech.edu
[2] Graduate Research Assistant, School of Aerospace Engineering
[3] Research Engineer, School of Aerospace Engineering
[4] Professor and William R. T. Oakes, Jr. School Chair, School of Aerospace Engineering

are most efficient within a specific range of power levels and on certain propellants, *e.g.*, xenon and krypton, so it is unclear how to best design HETs for different power levels and propellants. Second, the vacuum facility background pressure during HET experiments has been shown to affect HET performance [1-6], and the background pressure is orders of magnitude greater than that in space, so it is unclear how to relate HET performance on the ground to performance in space.

The conventional wisdom is that in the absence of a fully predictive HET model, progress on these two fronts must be made incrementally through experiments, which is very costly. For extending HET design to different power levels, this includes considering alternative HET designs [7-11] and improving them over time, while for developing HET designs for different propellants, this may include checking whether small design changes can improve HET performance on different propellants [12-15]. In addition, for pressure facility effects, this incremental progress has typically been achieved by separately characterizing the dependence of HET performance on the background pressure for different thrusters and by building newer vacuum chambers with higher pumping speeds. In addition, vacuum chambers with even higher pumping speeds than the current state-of-the-art will be needed to flight qualify high-power (> 20 kW) HETs.

Alternative approaches that do not rely on a complete understanding of HET physics are thus necessary to reduce the costs of solving the problems of HET scaling and pressure facility effects. To that end, this work presents a robust nondimensionalization of the HET discharge and facility effects. Even in the absence of a fully predictive HET model, a robust nondimensional framework can capture all the relevant physics of the HET and facility effects.

There have been several attempts to use nondimensional parameters to derive theoretical HET scaling laws [16-21], and similarity theory has also been developed for other low-temperature plasma devices [22-24]. Early work by Morozov [16] defined the ratio of the ionization mean free path to the channel length as a key nondimensional parameter and found that thruster efficiency was largely a function of just this one parameter across HET operation with different propellants. Ref. 16 also identified the ratio of the ionization energy to the discharge voltage as an important nondimensional parameter but acknowledged that more nondimensional parameters influenced the discharge. Later, Ref. 17 considered the ratio of the electron Larmor radius to the channel length as a fundamental nondimensional parameter, and Ref. 20 considered the ratio of the electron cyclotron frequency to the classical electron-neutral collision frequency.

However, given the numerous physical phenomena in a HET, more nondimensional parameters are required to describe the nondimensional HET discharge accurately. In particular, given the significance of anomalous electron transport (AET) in the HET discharge and the absence of a closure model for it, an accurate nondimensionalization of the HET discharge must account for all physical phenomena that could contribute to AET. In addition, high-power HETs have operated at higher voltages and higher current densities than nominal values. As such, it is important to consider as many physical phenomena as is reasonable to evaluate how the relative importance of different phenomena may change in different regimes of HET operation. In addition to the typical phenomena considered in the nondimensional parameters of a HET discharge, our nondimensional approach will also be general enough to account for anomalous electron transport, doubly charged ions, induced magnetic field, and non-equilibrium effects.

After defining an independent set of nondimensional parameters, we will then present similarity laws for the HET discharge. These similarity laws describe how the discharge parameters and thruster size must change to have constant nondimensional parameters; exact similarity would ensure constant efficiencies across the discharge conditions or HET designs. We differentiate these from scaling laws, as theoretical scaling laws make some assumptions to describe how HET efficiency is a function of nondimensional parameters.

Regarding pressure facility effects, the dependence of thrust on the background pressure has received the most attention, but the background pressure is also known to affect HET stability [5,6], discharge current [1], and lifetime [25]. Different HETs and different discharge conditions on the same HET have different pressure dependences on thrust [1-6, 26, 27], which complicates defining a criterion for an acceptable background pressure for qualification testing. However, there has been little effort to reconcile the different pressure dependences on thrust. For this purpose, we will define nondimensional parameters to describe facility effects and present a nondimensional framework to analyze existing pressure studies. Such a method can be used to experimentally determine a nondimensional correction to thrust as a function of background pressure that is applicable to a wide range of discharge conditions.

The paper is organized as follows. Section II will present the nondimensional HET parameters, justify the use of these nondimensional parameters by presenting the nondimensional fluid description of a HET, and define the nondimensional facility parameters. In Section III, we will describe the nondimensional framework used to analyze pressure studies, and Section IV will show similarity laws based on the nondimensional HET parameters that can be used to scale the HET discharge condition and HET size between discharge powers and propellants. Lastly, in Section V, we will apply the nondimensional to existing pressure studies and discuss the results with regard to experimental design and the possibility of reducing the dimensionality of HET pressure facility effects.

II. Theory

A. Nondimensional HET Discharge

The nondimensionalization of the HET discharge is carried out in three steps: First, determine the set of parameters, i.e., operating condition, that determines the dimensional HET discharge; second, define the reference plasma properties as a function of the operating condition; third, define an independent set of nondimensional parameters as a function of the reference plasma properties that satisfy the Buckingham π Theorem. After these three steps, we then present the nondimensional fluid equations of electrons, ions, and neutrals to see the qualitative effect of the nondimensional parameters on the HET discharge dynamics. We choose to follow the above approach, instead of first nondimensionalizing the fluid equations and seeing which nondimensional parameters appear, to account for kinetic and electromagnetic effects that would not be captured in the typical fluid formulation of a HET discharge. However, it will be shown in Section II.B.1 that the nondimensionalization fluid equations in a HET are completely described by the nondimensional parameters defined in this section. In addition, the nondimensional kinetic equations in a HET, found in Refs. 21 and 28, are also completely defined by the nondimensional parameters defined in this section.

We group the parameters that define the dimensional operating condition into the following four groups, shown in Tables 1-4: discharge parameters, channel parameters, cathode parameters, and propellant parameters. Table 1 includes the channel wall potential for the case of a conducting channel wall where a known bias can be applied. The channel parameters are those of an annular discharge channel, and if alternative geometries are used, then additional parameters should be specified. We note that $R_{kp} = 0$ for a center-mounted cathode and that σ_{SEE} depends on the propellant and local reduced electric field at the wall [29]. Regarding the cathode parameters, we acknowledge the importance of the internal parameters of the cathode, such as the work function of the emitter and the internal geometry of the cathode. Still, we will exclude these parameters from the main analysis because they are typically not reported alongside HET data. Regarding the propellant parameters, the second ionization energy, excitation energies, and excitation cross sections are expected to be important but are neglected for the main analysis because their inclusion in the electron energy equation is a straightforward extension from the formulation used for the first ionization. Lastly, we define the set of fundamental constants in Table 5.

Table 1. Dimensional discharge parameters

Variable	Definition
V_d	Discharge voltage
$\dot{m}_a$	Anode mass flow rate
$\vec{B}(r,z)$	Magnetic field topology
T_w	Thruster wall temperature
ϕ_B	Thruster body potential
ϕ_w	Channel wall potential

Table 2. Dimensional channel parameters

Variable	Definition
L_{ch}	Channel length
W_{ch}	Channel width
D_{ch}	Channel mean diameter
σ_{SEE}	Secondary electron emission coefficient of channel wall material

Table 3. Dimensional cathode parameters

Variable	Definition
$\dot{m}_c$	Cathode flow rate
W_{kp}	Keeper inner diameter at keeper exit plane
R_{kp}	Radial location of the keeper centerline with respect to thruster centerline

Table 4. Dimensional propellant parameters

Variable	Definition
m_p	Propellant mass
ε_{iz1}	First ionization energy
$\sigma_{iz1}(E)$	Electron-impact first ionization cross section function
$\sigma_{iz2}(E)$	Electron-impact second ionization cross section function
$\sigma_{en}(E)$	Electron-neutral elastic collision cross section function
$\sigma_{CEX}(E)$	Charge exchange cross section as a function
σ_{nn}	Neutral-neutral elastic collision cross section

Table 5. Fundamental constants

Variable	Definition
m_e	Electron mass
e	Elementary charge
k_B	Boltzmann constant
ε_0	Vacuum permittivity
μ_0	Vacuum permeability

The definition of the reference plasma properties is the most important step for obtaining accurate relationships between the operating condition and physical phenomena in the HET. We define two reference applied magnetic field strengths, the maximum radial magnetic field along the channel centerline, B_{r0}, and the axial magnetic field along the channel centerline at the location of B_{r0}, B_{z0}. The reference electric field is $E_0 = V_d/L_{ch}$, and we define the reference temperatures for electrons and neutrals as $T_{e0} = \frac{V_d}{10}$ and $T_{n0} = T_w$, respectively, where T_{e0} is in eV. We also define the reference electron temperature at the channel wall as $T_{ew,0} = T_{e0}$ for unshielded HETs and $T_{ew} = \frac{T_{e0}}{10}$ for magnetically shielded HETs. We then define the reference neutral velocity, the two reference ion velocities, and the three reference electron velocities as

$$u_{n0} = \sqrt{\frac{8k_B T_w}{\pi m_p}},\ u_{i0} = \sqrt{\frac{2eV_d}{m_p}},\ u_{iw0} = \sqrt{\frac{eT_{ew}}{m_p}},\ u_{e\theta 0} = \frac{V_d}{L_{ch}B_{r0}},\ u_{e,th0} = \sqrt{\frac{8eT_{e0}}{\pi m_e}} \tag{1}$$

where u_{i0} is the reference axial ion velocity, u_{iw} is the reference Bohm velocity, $u_{e\theta}$ is the reference azimuthal electron drift velocity, and $u_{e,th0}$ is the reference electron thermal velocity. We also define the reference axial electron drift velocity as $u_{ez} = u_{i0}$. In the absence of a closure model for anomalous electron transport, we believe that u_{i0} is the most representative reference value for the axial electron drift velocity given quasineutrality and current conservation in the plume. From the reference velocities, we define the reference neutral and ion number densities in the channel as

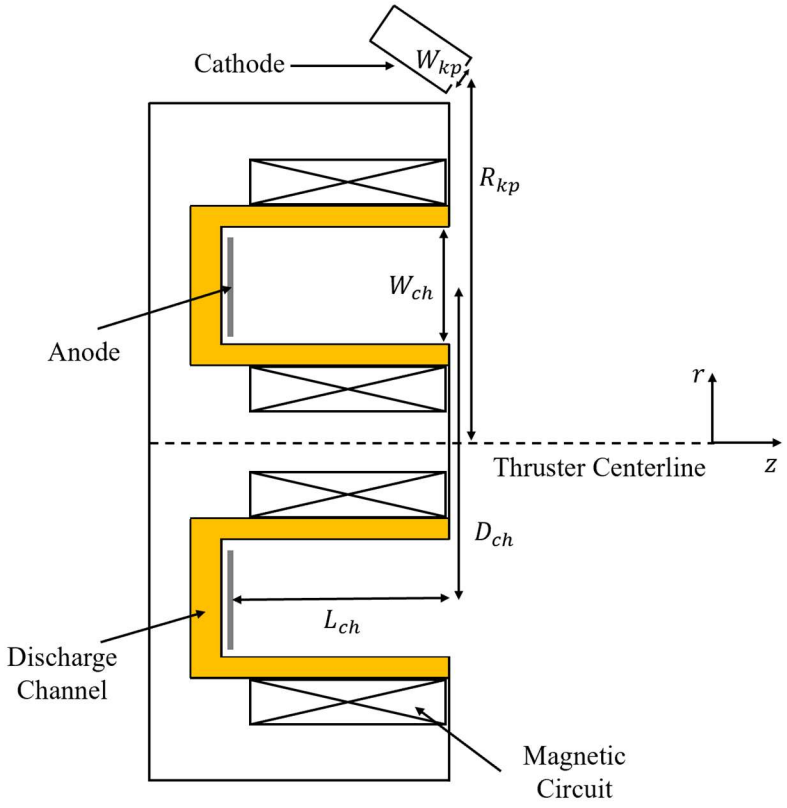

Figure 1. Schematic of an annular HET. Geometric parameters L_{ch}, W_{ch}, D_{ch}, W_{kp}, and R_{kp} are shown.

$$n_{n0} = \frac{\dot{m}_a}{W_{ch}D_{ch}\sqrt{8\pi m_p k_B T_w}}, n_{i0} = \frac{\dot{m}_a}{\pi W_{ch}D_{ch}\sqrt{2m_p e V_d}} \quad (2)$$

and we define the reference electron density in the channel as $n_{e0} = n_{i0}$.

Next, we define the reference first ionization rate coefficient as $k_{iz1,0} = \langle \sigma_{iz1} v_e \rangle (T_e)$, where $\langle \sigma_{iz1} v_e \rangle (T_{e0})$ represents the product of σ_{iz1} and the electron velocity, averaged over a Maxwell-Boltzmann electron speed distribution evaluated at an electron temperature of T_{e0}. The rate coefficients for second ionization and elastic electron neutral collisions, $k_{iz2,0}$ and k_{en0}, are defined similarly. We also define the reference charge exchange rate coefficient as $k_{CEX,0} = \sigma_{CEX}|_{u_{i0}} u_{i0}$, where $\sigma_{CEX}|_{u_{i0}}$ is equal to σ_{CEX} evaluated at u_{i0}, and the reference electron-electron Coulomb collision rate coefficient is $k_{ee0} = \frac{1}{\varepsilon_0^2}\sqrt{\frac{e^5}{\pi^3 m_e T_{e0}^3}}$. Lastly, we consider the reference magnetic field induced by the reference Hall current. To first order, we approximate the Hall current as an infinitely thin current loop with current $e n_{e0} u_{e\theta 0} L_{Br} W_{ch}$ and diameter D_{ch}, which creates a reference induced magnetic field at the thruster centerline of

$$B_{ind} = \frac{\mu_0 e n_{e0} u_{e\theta 0} L_{Br} W_{ch}}{D_{ch}} = \frac{\mu_0 \dot{m}_a}{D_{ch}^2 B_{r0}}\sqrt{\frac{eV_d}{2m_p}}. \quad (3)$$

Arriving at the nondimensional HET parameters, we again separate them into five groups, namely discharge parameters (A_1-A_8), channel parameters (T_1-T_3), cathode coupling parameters (C_1-C_3), propellant parameters (P_1-P_6), and electrical configuration parameters (B_1 and B_2). These parameters are defined in Table 6 and are expressed in terms of the discharge condition, assuming $n_{e0} = n_{i0}$, $u_{ez0} = u_{i0}$, and $T_e = \frac{V_d}{10}$. For the nondimensional discharge parameters, we preliminarily define them as ratios of characteristic plasma parameters, where in addition to the ones defined above, we also define the reference neutral ionization mean free path, $\lambda_{iz0} \equiv \frac{u_{n0}}{n_{e0} k_{iz}}$, the reference electron cyclotron frequency, $\omega_{ce0} \equiv \frac{eB_{r0}}{m_e}$, the reference plasma frequency, $\omega_{pe} \equiv \sqrt{\frac{m_e n_{e0}}{\varepsilon_0 e^2}}$, the reference electron Larmor radius, $r_{e0} \equiv \frac{u_{e,th0}}{\omega_{ce}}$, the reference mean free path for electron-electron Coulomb collisions, $\lambda_{ee} \equiv \frac{u_{ez}}{n_{e0} k_{ee}}$, and the reference mean free path for neutral-neutral elastic collisions, $\lambda_{nn} \equiv \frac{1}{n_{n0}\sigma_{nn}}$. For the propellant parameters, to define nondimensional collision cross-section functions, we first define a reference collisional cross-section, $\sigma_{en}(U^0)$, where $U^0 = 10$ eV is chosen arbitrarily for the reference energy. While we exclude internal cathode parameters from future consideration, to further nondimensionalize the cathode behavior, we could include the aspect ratios of the internal cathode geometry, and the ratio of the emitter work function to the HET's discharge voltage.

It can be shown that the set of nondimensional parameters defined in Table 6 is independent. In addition, without loss of generalization, the HET discharge can be defined by 22 physical variables if we only consider σ_{nn}, $k_{iz1,0}$, and k_{ee} among the collisional variables, consider $k_B T_w$ as a single variable, and only consider B_{r0} and B_{z0} instead of the entire magnetic field topology. Then, the 18 nondimensional variables of A_1-A_8, C_1-C_3, T_1-T_3, P_1, P_2, B_1, and B_2 satisfy the condition of the Buckingham π theorem for the minimum set of independent parameters that describe the HET discharge, considering the four base dimensions of length, time, mass, and electrical current. We also note that the extension of the nondimensional parameters to include molecular propellants and additional collisional processes is straightforward.

Table 6. Nondimensional variables of a HET. A_1-A_7 are defined by ratios of characteristic properties. A_1-A_7 are then expressed as a function of the discharge conditions, which requires assumptions to relate the characteristic properties to the HET discharge condition. A_8-B_2 are defined by the HET discharge condition.

Nondimensional Variable	Definition in terms of characteristic properties	Expression in terms of discharge condition
A_1	$\frac{\lambda_{iz0}}{L_{ch}}$	$\frac{W_{ch}D_{ch}\sqrt{16\pi k_B T_w eV_d}}{\dot{m}_a k_{iz1,0} L_{ch}}$
A_2	$\frac{r_{e0}}{L_{ch}}$	$\frac{1}{B_0 L_{ch}}\sqrt{\frac{4m_e V_d}{5\pi e}}$
A_3	$\frac{\omega_{pe0}}{\omega_{ce0}}$	$\frac{1}{B_{r0}}\sqrt{\frac{m_e \dot{m}_a}{\varepsilon_0 \pi W_{ch} D_{ch}\sqrt{2m_p eV_d}}}$
A_4	$\frac{u_{n0}}{u_{i0}}$	$\sqrt{\frac{4k_B T_w}{\pi eV_d}}$
A_5	$\frac{\lambda_{ee0}}{L_{ch}}$	$\frac{W_{ch}D_{ch}}{\dot{m}_a}\frac{\varepsilon_0^2}{L_{ch}}\sqrt{\frac{\pi^5 m_e V_d^5}{250e^3}}$
A_6	$\frac{\lambda_{nn0}}{L_{ch}}$	$\frac{W_{ch}D_{ch}\sqrt{8\pi m_p k_B T_w}}{L_{ch}\sigma_{nn}\dot{m}_a}$
A_7	$\frac{B_{ind}}{B_{r0}}$	$\frac{\mu_0 \dot{m}_a}{\pi D_{ch}^2 B_{r0}^2}\sqrt{\frac{eV_d}{2m_p}}$
A_8	-	$\frac{B_{r0}}{B_{z0}}$
C_1	-	$\frac{\dot{m}_c}{\dot{m}_a}$
C_2	-	$\frac{R_{kp}}{W_{kp}}$
C_3	-	$\frac{D_{ch}}{W_{kp}}$
T_1	-	$\frac{L_{ch}}{W_{ch}}$
T_2	-	$\frac{W_{ch}}{D_{ch}}$
T_3	-	$1-\sigma_{SEE}$
P_1	-	$\frac{m_e}{m_p}$
P_2	-	$\frac{\varepsilon_{iz}}{V_d}$
P_3	-	$\frac{\sigma_{iz1}(E)}{\sigma_{en}(U^0)}$
P_4	-	$\frac{\sigma_{en}(E)}{\sigma_{en}(U^0)}$
P_5	-	$\frac{\sigma_{iz2}(E)}{\sigma_{en}(U^0)}$
P_6	-	$\frac{\sigma_{CEX}(E)}{\sigma_{en}(U^0)}$
B_1	-	$\frac{\phi_B}{V_d}$
B_2	-	$\frac{\phi_w}{V_d}$

In addition, it is important to consider the nondimensional magnetic field topology defined by $A_9 \equiv \frac{\partial B_r^*}{\partial r^*} = \frac{D_{ch}}{B_{r0}}\frac{\partial B_r}{\partial r}$, $A_{10} \equiv \frac{\partial B_z^*}{\partial z^*} = \frac{L_{ch}}{B_{z0}}\frac{\partial B_z}{\partial z}$, $A_{11} \equiv \frac{\partial B_r^*}{\partial z^*} = \frac{L_{ch}}{B_{r0}}\frac{\partial B_r}{\partial z}$, and $A_{12} \equiv \frac{\partial B_z^*}{\partial r^*} = \frac{D_{ch}}{B_{z0}}\frac{\partial B_z}{\partial r}$, where $z^* \equiv \frac{z}{L_{ch}}$ is the nondimensional axial coordinate and $r^* \equiv \frac{r}{D_{ch}}$ is the nondimensional radial coordinate. $A_8T_1T_2$ must be the same between two magnetic fields for them to have the same nondimensional topology, since $A_8T_1T_2$ governs the nondimensional divergence-free condition of the magnetic field. It will also be useful to define some extra nondimensional parameters for the propellant. For the propellant, we can define $P_7 \equiv \frac{k_{iz1,0}}{k_{en}}$, $P_8 \equiv \frac{k_{iz1,0}}{k_{iz2,0}}$, $P_9 \equiv \frac{k_{iz1,0}}{k_{CEX,0}}$, $k_{iz1}^*(T_e^*) = \frac{k_{iz1}(T_e)}{k_{iz0}}$, $k_{iz2}^*(T_e^*) = \frac{k_{iz}\ (T_e)}{k_{iz2,0}}$, $k_{en}^*(T_e^*) = \frac{k_{en}(T_e)}{k_{en0}}$, and $k_{CEX}^*(u_i^*) = \frac{k_{CEX}(u_i)}{k_{CEX,0}}$, which depend on P_3, P_4, P_5, and P_6 for a given T_{e0} and u_{i0}, and where $T_e^* = \frac{T_e}{T_{e0}}$ and $u_i^* = \frac{u_i}{u_{i0}}$ are the nondimensional electron temperature and ion velocity.

Furthermore, the expressions in Table 6 for A_1, A_2, A_3, A_5, and A_7 depend on the definitions of $n_{e0} = n_{i0}$, $u_{ez} = u_{i0}$, and $T_{e0} = \frac{V_d}{10}$. These nondimensional parameters could be corrected by factors of $\frac{n_{e0}}{n_{i0}}$, $\frac{u_{ez}}{u_{i0}}$, and $\frac{10\ _{e0}}{V_d}$, which could be found from a 0D electron model of the thruster discharge. However, such corrections would be functions of the previously defined nondimensional parameters. As a result, if we are only concerned with defining a set of independent nondimensional parameters that fully describe the HET discharge, then corrections for $\frac{n_{e0}}{n_{i0}}$, $\frac{u_{ez}}{u_{i0}}$, and $\frac{10T_{e0}}{V_d}$ are not necessary, but if we want to accurately describe how nondimensional HET discharge phenomena scale with dimensional HET operating parameters, then the corrections for $\frac{n_{e0}}{n_{i0}}$, $\frac{u_{ez0}}{u_{i0}}$, and $\frac{T_{e0}}{V_d}$ are necessary. As such, when nondimensionalizing the fluid equations in the next section, we will not assume definitions for $\frac{n_{e0}}{n_{i0}}$, $\frac{u_{ez}}{u_{i0}}$, and $\frac{T_{e0}}{V_d}$.

Before continuing, it is useful to consider how other nondimensional parameters that may be important are related to the parameters defined in Table 6. For example, the reference classical electron Hall parameter is $\frac{\omega_{ce}}{n_{n0}k_{en}} = \frac{A_1P_7}{A_2\sqrt{P_1}}$, the reference anomalous electron Hall parameter is $\frac{u_{e\theta}}{u_{ez}} \sim \frac{A_2}{\sqrt{P_1}}$, the ratio of the reference Debye length to the channel length is $\frac{\lambda_{De,0}}{L_{ch}} \sim \frac{A_2}{A_3}$, the reference azimuthal electron Mach number is $\frac{u_{e\theta}}{u_{et\ ,0}} \sim A_2$, and the reference number of neutrals in the channel is $L_{ch}W_{ch}D_{ch}n_{n0} = \frac{A_5A_3^4T_1^2}{A_2^4A_4^4P_1^2T_2}$.

B. Nondimensional Analysis of HET Dynamics

1. Nondimensional Fluid Equations for HET Discharge

In this section, we will present the nondimensional fluid equations of the HET discharge to show that the nondimensional parameters defined in Section II.A do, in fact, describe the nondimensional fluid description of a HET discharge. The main caveat against focusing on the fluid description is that it does account for kinetic phenomena or finite-sheath effects. However, finite-sheath effects should be accounted for in our nondimensional parameters because $\frac{\lambda_{De,0}}{L_{ch}} = \frac{A_2}{A_3}$. In addition, non-Maxwellian kinetic effects should also be accounted for in our nondimensional parameters because $\frac{A_5u_{ez}}{u_{i0}}$ and A_6 are the reference Knudsen numbers for electrons and neutrals, the reference ion Knudsen number is $\frac{\lambda_{ii,0}}{L_{ch}} = \frac{A_5}{\sqrt{P_1}}$. Also, even though we assume an isotropic electron pressure tensor in the fluid equations, A_5

should govern the relaxation to an isotropic electron pressure tensor and $\frac{u_{ez0}\omega_{ce0}}{L_{ch}} \sim \frac{1}{A_2\sqrt{P_1}}\frac{u_{ez}}{u_{i0}}$ should govern the relaxation to a gyrotropic electron pressure tensor [30].

Furthermore, even though a full treatment of kinetic instabilities in HETs is out of the scope of this work, it can be shown that $\frac{u_{e\theta 0}}{u_{eth,0}} \sim A_2$, A_3, and P_1 govern the dispersion relation of the electron cyclotron drift instability (ECDI) presented in Ref. 31, so we believe the nondimensional behavior of kinetic instabilities in a HET should be described by our defined set of HET nondimensional parameters. Indeed, it is known that artificially changing the vacuum permittivity or ion mass in simulations can affect the behavior of the ECDI [32]. Lastly, fluid instabilities are also prevalent in a HET, but if our nondimensional parameters can describe the nondimensional fluid description of the HET discharge, then they can also describe the behavior of the nondimensional fluid instabilities in a HET.

To gain a preliminary understanding of the nondimensional HET dynamics, it is sufficient to consider the following conservation equations: continuity equations of electrons, ions, and neutrals, axial momentum equation of electrons and ions, radial and azimuthal momentum equations of electrons, and the electron energy equation. To incorporate wall effects directly into the conservation equations instead of as boundary conditions and for simplicity, we consider 1D models for all conservation equations except for the radial electron momentum equation. In addition, we are primarily interested in describing global phenomena, so our reference length scale is channel length, and the reference time scale is that of neutral convection. We note that alternative length and time scales would be useful to find the nondimensional parameters that govern small-scale phenomena [28].

For the 1D models we used Ref. 33 as a reference for the continuity and momentum equations and Ref. 34 as a reference for the electron energy equation. For the continuity equations, we expanded on Ref. 33 by including single-ionization of ions and charge-exchange collisions, such that the nondimensional 1D neutral, ion, and electron continuity equations are

$$\frac{\partial n_n^*}{\partial t^*} + \frac{\partial (n_n^* u_{nz}^*)}{\partial z^*} = -\frac{n_{e0}}{n_{i0}A_1} n_e^* n_n^* k_{iz1}^* + \frac{1}{A_1 P_9} n_i^* n_n^* k_{CEX}^* + \frac{n_{e0}T_1}{n_{i0}} \sqrt{\frac{T_{ew,0}}{8V_d}} \Gamma_{iw}^*, \tag{4}$$

$$A_4 \frac{\partial n_i^*}{\partial t^*} + \frac{\partial (n_i^* u_{iz}^*)}{\partial z^*} = \frac{n_{e0}}{n_{i0}A_1} n_e^* n_n^* k_{iz1}^* - \frac{n_{e0}A_4}{n_{i0}A_1 P_8} n_i^* n_e^* k_{iz2}^* - \frac{1}{A_1 P_9} n_i^* n_n^* k_{CEX}^* - \frac{n_{e0}T_1}{n_{i0}} \sqrt{\frac{T_{ew,0}}{8V_d}} \Gamma_{iw}^* \tag{5}$$

$$A_4 \frac{\partial n_e^*}{\partial t^*} + \frac{u_{ez0}}{u_{i0}} \frac{\partial (n_e^* u_{ez}^*)}{\partial z^*} = \frac{1}{A_1} n_e^* n_n^* k_{iz1}^* + \frac{A_4}{A_1 P_8} n_i^* n_e^* k_{iz2}^* - T_1 \sqrt{\frac{T_{ew,0}}{8V_d}} \Gamma_{iw}^*, \tag{6}$$

where $n_n^* = \frac{n_n}{n_{n0}}$ is the nondimensional neutral density, $n_i^* = \frac{n_i}{n_{i0}}$ is the nondimensional ion density, $n_e^* = \frac{n_e}{n_{i0}}$ is the nondimensional electron density, $u_{nz}^* = \frac{u_{nz}}{u_{n0}}$ is the nondimensional axial neutral velocity, $u_{iz}^* = \frac{u_{iz}}{u_{i0}}$ is the nondimensional axial ion velocity, $u_{ez}^* = \frac{u_{ez}}{u_{i0}}$ is the nondimensional axial electron velocity, $t^* = \frac{t u_{n0}}{L_{ch}}$ is the nondimensional time, and $\Gamma_{iw}^* = \frac{2\Gamma_{iw}}{n_{e0}u_{iw0}}$ is the nondimensional ion flux to the channel walls. For the ion momentum equation, unlike in Ref. 33, we do not account for the dispersion of axial ion velocities or for the neutral velocity, but we do account for the same collisional processes in the continuity equations, such that the nondimensional 1D ion momentum equation in conservative form is

$$A_4\frac{\partial(n_i^*u_{iz}^*)}{\partial t^*}+\frac{\partial\left(n_i^*{u_{iz}^*}^2\right)}{\partial z^*}=\frac{1}{2}n_i^*E_z^*\ -\frac{n_{e0}A_4}{n_{i0}A_1P_8}n_e^*n_i^*u_{iz}^*k_{iz2}^*-\frac{1}{A_1P_9}n_i^*n_n^*u_{iz}^*k_{CEX}^*-\frac{n_{e0}T_1}{n_{i0}}\sqrt{\frac{T_{ew,0}}{8V_d}}u_{iz}^*\Gamma_{iw}^*, \tag{7}$$

where $E_z^*=\frac{E_z}{E_0}$ is the nondimensional axial electric field.

Regarding the 1D axial and azimuthal electron momentum equations, we have neglected the momentum gained from ionization of ions, and we have included the dominant inertia terms [35, 36], such that the nondimensional 1D axial and azimuthal electron momentum equations are

$$P_1A_4\frac{u_{ez0}}{u_{i0}}\frac{\partial(n_e^*u_{ez}^*)}{\partial t^*}+P_1\left(\frac{u_{ez0}}{u_{i0}}\right)^2\frac{\partial\left(n_e^*{u_{ez}^*}^2\right)}{\partial z^*}=-\frac{1}{2}n_e^*E_z^*\ +\frac{1}{2}n_e^*u_{e\theta}^*B_r^*\ -\frac{T_{e0}}{2V_d}\frac{\partial(n_e^*T_e^*)}{\partial z^*}$$
$$-\frac{u_{ez0}P_1}{u_{i0}A_1P_7}n_e^*n_n^*u_{ez}^*k_{en}^*-\frac{u_{ez0}P_1T_1}{u_{i0}T_3}\sqrt{\frac{T_{ew,0}}{8V_d}}u_{ez}^*\Gamma_{iw}^*, \tag{8}$$

$$\frac{A_2^2A_45\pi u_{i0}}{4u_{ez0}}\frac{\partial(n_e^*u_{e\theta}^*)}{\partial t^*}+\frac{A_2^25\pi}{4}\frac{\partial(n_e^*u_{ez}^*u_{e\theta}^*)}{\partial z^*}=-n_e^*u_{ez}^*B^*\ -n_e^*u_{e\theta}^*\nu_a^*$$
$$-\frac{5\pi A_2^2u_{i0}}{4A_1P_7u_{ez0}}n_e^*n_n^*u_{e\theta}^*k_{en}^*-\sqrt{\frac{T_{ew,0}}{8V_d}}\frac{5\pi A_2^2T_1u_{i0}}{4T_3u_{ez0}}u_{e\theta}^*\Gamma_{iw}^*, \tag{9}$$

where $u_{e\theta}^*=\frac{u_{e\theta}}{u_{e\theta}}$ is the nondimensional azimuthal electron drift velocity, $B_r^*=\frac{B_r}{B_{r0}}$ is the nondimensional radial magnetic field, and $\nu_a^*=\frac{\nu_au_{e\theta0}}{\omega_{ce0}u_{ez}}$ is the nondimensional anomalous electron collision frequency. For simplicity, we neglect ion-electron momentum transfer collisions in the nondimensional momentum equations. For the radial electron momentum equation, we include the centrifugal force and a non-negligible axial magnetic field, such that the nondimensional radial electron momentum equation is

$$\frac{2A_4P_1u_{ez0}}{u_{i0}}\frac{\partial(n_e^*u_{er}^*)}{\partial t^*}-\frac{A_2^2A_8T_1T_25\pi}{4}\frac{n_e^*u_{e\theta}^{*2}}{r^*}=-n_e^*E_r^*-n_e^*u_{e\theta}^*B_z^*$$
$$-\frac{T_{e0}A_8T_1}{V_d}\frac{\partial(n_e^*T_e^*)}{\partial r^*}+\frac{2P_1u_{ez0}}{A_1P_7u_{i0}}n_e^*n_n^*u_{er}^*k_{en}^*, \tag{10}$$

where $E_r^*=\frac{E_rB_{r0}}{E_0B_{z0}}$ is the nondimensional radial electric field, $B_z^*=\frac{B_z}{B_{z0}}$ is the nondimensional axial magnetic field, and $u_{er}^*=\frac{u_{er}B_{r0}}{u_{ez}B_{z0}}$ is the nondimensional radial electron velocity. In addition, to accurately represent the radial dynamics within the discharge channel, we define $\frac{\partial}{\partial r^*}=W_{ch}\frac{\partial}{\partial r}$. Lastly, to the 1D electron energy equation in Ref. 34, we add cross-field thermal conductivity and the loss terms due to thermalization with ions and neutrals, but we neglect electron inertia, such that the nondimensional 1D electron energy equation is

$$\frac{A_4 u_{i0} T_{e0}}{u_{ez0} V_d} \frac{\partial\left(\frac{3}{2} n_e^* T_e^*\right)}{\partial t^*} + \frac{T_{e0}}{V_d} \frac{\partial\left(\frac{5}{2} n_e^* u_{ez}^* T_e^*\right)}{\partial z^*} = n_e^* u_{ez}^* E_z^* - \frac{P_2 u_{i0}}{A_1 u_{ez0}} n_e^* n_n^* k_{iz1}$$
$$- \left(\frac{T_{ew,0}}{V_d}\right)^{\frac{3}{2}} \frac{T_1}{T_3\sqrt{8}} \left[1 + \ln\left(T_3 \sqrt{\frac{1}{2\pi P_1}}\right)\right] \Gamma_{iw}^* \varepsilon_w^* - \frac{A_2 u_{i0}}{A_1 P_7 u_{ez0}} \frac{\partial}{\partial z^*} \left(\kappa_z^* \frac{\partial T_e^*}{\partial z^*}\right)$$
$$- \frac{P_1 n_{i0} T_{e0}}{A_5 n_{e0} V_d \sqrt{2}} n_e^* n_i^* k_{ei,\varepsilon}^* T_e^* - \frac{P_1 u_{i0} T_{e0}}{A_1 P_7 u_{ez0} V_d} n_e^* n_n^* k_{en,\varepsilon}^* T_e^*, \tag{11}$$

where $\varepsilon_w^* = \frac{\varepsilon_w}{T_{ew,0}\left[1+\ln\ (1-\sigma_{SEE})\sqrt{\frac{m_p}{2\pi m_e}}\right]}$ is the nondimensional average electron energy lost at the channel walls, $\kappa_z^* = \frac{\kappa_z B_{r0}^2}{m_e n_{e0} T_{e0} n_{n0} k_{en0}}$ is the nondimensional classical cross-field electron thermal conductivity, $k_{ei,\varepsilon}^* = \frac{k_{ei,\varepsilon}\sqrt{2} m_p}{k_{ee0} m_e}$ is the nondimensional electron-ion energy transfer collision rate, and $k_{en,\varepsilon}^* = \frac{k_{en,\varepsilon} m_p}{k_{en}\ m_e}$ is the nondimensional electron-neutral energy transfer collision rate. In Eq. 11, without loss of generality, we have neglected inelastic losses due to excitation and ionization of ions, only included electron-neutral collisions to define κ_z^*, and assumed negligible neutral and ion temperatures.

2. Physical Relevance of Nondimensional Discharge Parameters

From Eqs. 4-11, the nondimensional parameters that define the axisymmetric nondimensional fluid description of the HET discharge are A_1, A_2, A_4, A_5, A_8, T_1, T_2, T_3, P_1, P_2, P_7, P_8, and P_9. In particular, ratios of characteristic processes in a HET in terms of the nondimensional parameters are shown in Table 7. Using characteristic HET parameters of $V_d = 300\,V$, $B_{r0} = 200\,G$, $\frac{\dot{m}_a}{\pi W_{ch} D_{ch}} = 10^{-3}\,\frac{kg}{s \cdot m^2}$, $L_{ch} = 30\,mm$, $W_{ch} = 30\,mm$, $D_{ch} = 100$, $T_w = 500\,K$, $\sigma_{SEE} = 0.5$, and xenon as the propellant, then $A_1 = 0.28$, $A_2 = 0.11$, $A_4 = 1.4 \times 10^{-2}$, $T_1 = 1$, $T_2 = 0.3$, $T_3 = 0.5$, $P_1 = 4.1 \times 10^{-6}$, $P_2 = 0.04$, $P_7 = 0.22$, $P_8 = 2.4$, $P_9 = 7.3$. To calculate A_1, P_7, and P_9 for xenon, we used the expressions in Ref. 37 of $\sigma_{CEX} = 10^{-18}\,m^2$, $k_{iz}\ [m^3/s] \approx 10^{-20}\left[-(1.031 \times 10^{-4}) T_{eV}^2 + 6.386 \exp\left(-\frac{12.127}{T_{eV}}\right)\right]\left(\frac{8eT_{eV}}{\pi m_e}\right)^{1/2}$, and $k_{en}[m^3/s] \approx 6.6 \times 10^{-19}\left[\frac{\frac{T_{eV}}{4}-0.1}{1+\left(\frac{T_{eV}}{4}\right)^{1.6}}\right]\left(\frac{8eT_{eV}}{\pi m_e}\right)^{1/2}$ and evaluated them at $T_{eV} =$ 30 eV; this resulted in $k_{iz1,0} = 1.53 \times 10^{-13}\ m^3/s$ and $k_{en0} = 6.95 \times 10^{-1}\ \ m^3/s$. To calculate P_8, we used cross-sections for ionization of xenon ions from Ref. 38 and assumed a Maxwellian electron speed distribution at an electron temperature of 30 eV, which resulted in $k_{iz2,0} = \ 6.39 \times 10^{-14}\ m^3/s$. Plugging the above values into the expressions in Table 7, we arrive at the typical findings that electron inertia, classical momentum-transfer and energy-transfer collisions, and classical cross-field heat flux are negligible. In this case, the axisymmetric nondimensional fluid description of the HET discharge would be described entirely by A_1, A_4, A_8, T_1, T_3, P_2, P_8, and P_9 in addition to the known dependence on the nondimensional magnetic field topology. In particular, the neutral and ion dynamics would be entirely described by A_1, A_4, T_1, P_8, and P_9, the electron momentum dynamics would be governed by A_1, A_8, T_1, and T_3, and the electron energy dynamics would be governed A_1, T_1, T_3, and P_2.

However, there are several considerations that may change the relevance of different parameters. First, it has been shown that magnetically shielded (MS) HETs have a weak dependence on the wall material [39, 40], such that T_3 is no longer an important parameter for MS HETs. Second, a combination of C_1 and C_2 should influence the nondimensional cathode coupling voltage. Third, it has been shown that in certain parts of the HET discharge, electron

inertia is non-negligible in the azimuthal and radial electron momentum equations [35, 41], such that A_2 and T_2 are not entirely negligible for the fluid description of electrons. Fourth, from the previous discussion on the ECDI, anomalous electron transport should have a non-negligible influence from A_2, A_3, and P_1. In fact, when nondimensionalizing the fluid equations on the time scale of the plasma frequency and length scale of the Debye length, Ref. 28, found that A_3 and P_1 governed the nondimensional equations. While not a universal trend, the scaling of $B_{r0} \sim \sqrt{\dot{m}_a}$ a at constant discharge voltage suggested by A_3 has been observed to minimize discharge current oscillations in the SPT-140 [1].

Table 7. Ratios of characteristic processes in a HET expressed by the nondimensional variables defined in Table 6. These characteristic processes are taken from the fluid equations, Eqs. 4-11, and are expressed using $\frac{n_{e0}}{n_{i0}}$, $\frac{u_{ez0}}{u_{i0}}$, $\frac{T_{e0}}{V_d}$, and $\frac{T_{ew,0}}{V_d}$ for generality.

Nondimensional Variable	Ratio of characteristic processes in a HET
$\sqrt{\frac{T_{ew,0}}{8V_d}}\frac{T_1 n_{e0}}{n_{i0}}$	$\frac{ion-wall\ recombination\ mean\ free\ path}{L_{ch}}$
$\sqrt{\frac{8V_d}{T_{ew,0}}}\frac{1}{A_1 T_1}$	$\frac{ionization\ rate\ of\ neutrals}{recombination\ rate\ of\ ions\ at\ walls}$
$\frac{P_8}{A_4}$	$\frac{ionization\ rate\ of\ neutrals}{ionization\ rate\ of\ ions}$
$\frac{2P_1 u_{ez0}}{A_1 P_7 u_{i0}}$	$\frac{classical\ axial\ electron\ resistivity}{axial\ Lorentz\ force}$
$\sqrt{\frac{T_{ew,0}}{8V_d}}\frac{2P_1 T_1 u_{ez0}}{T_3 u_{i0}}$	$\frac{axial\ electron\ resitivity\ due\ to\ wall\ collisions}{axial\ Lorentz\ force}$
$\frac{5\pi A_2^2}{4}$	$\frac{azimuthal\ electron\ inertia}{anomalous\ azimuthal\ electron\ resistivity}$
$\frac{5\pi A_2^2 u_{i0}}{4A_1 P_7 u_{ez0}}$	$\frac{classical\ azimuthal\ electron\ resistivity}{anomalous\ azimuthal\ electron\ resistivity}$
$\sqrt{\frac{T_{ew,0}}{8V_d}}\frac{5\pi A_2^2 T_1 u_{i0}}{4T_3 u_{ez0}}$	$\frac{azimuthal\ electron\ resitivity\ due\ to\ wall\ collisions}{anomalous\ azimuthal\ electron\ resistivity}$
$\frac{T_1 A_8 T_{e0}}{V_d}$	$\frac{radial\ electron\ pressure\ gradient}{radial\ Lorentz\ force}$
$\frac{5\pi A_2^2 A_8 T_1 T_2}{4}$	$\frac{electron\ centrifugal\ force}{radial\ Lorentz\ force}$
$\frac{P_2 u_{i0}}{A_1 u_{ez0}}$	$\frac{electron\ energy\ loss\ due\ to\ ionization\ of\ neutrals}{Joule\ heating\ of\ electrons}$
$\frac{A_2^2 u_{i0}}{A_1 P_7 u_{ez0}}$	$\frac{classical\ cross-field\ heat\ transport\ of\ electrons}{Joule\ heating\ of\ electrons}$
$\frac{P_1 n_{i0}}{A_5 n_{e0}\sqrt{2}}$	$\frac{electron-ion\ thermal\ relaxation\ time}{axial\ transit\ time\ of\ electrons}$
$\left(\frac{V_d}{T_{ew,0}}\right)^{3/2}\frac{P_2 T_3\sqrt{8}}{A_1 T_1\left[1+\ln\left(T_3\sqrt{\frac{1}{2\pi P_1}}\right)\right]}$	$\frac{electron\ energy\ lost\ to\ ionization}{electron\ energy\ lost\ to\ channel\ walls}$

In addition, A_4 influences the coupling between transit time oscillations of ions and neutrals as well as influencing the fraction of doubly charged ions. This may suggest that A_4 is of secondary importance, but it has been shown that the presence of doubly-charged ions can significantly affect anomalous electron transport [42]. Lastly, apart from

increasing the thrust density and the significance of the electron centrifugal force, a higher T_2 should decrease the distance between the cathode and the channel, which should affect cathode coupling. In conclusion, we expect the most physically significant nondimensional parameters to describe the HET discharge to be A_1, A_2, A_3 A_4, T_1, T_2, T_3, P_1, P_2, and P_8, in addition to the nondimensional magnetic field topology, which also defines A_8.

C. Nondimensionalization of Facility Effects

Analogously to the nondimensionalization of the HET discharge, the nondimensionalization of the facility effects is carried out in three steps; First, determine the set of parameters that determines the dimensional facility effects; second, define the reference facility properties as a function of the facility parameters; define an independent set of nondimensional parameters as a function of the reference facility properties and of the reference plasma properties of the HET discharge.

We consider a cylindrical vacuum chamber equipped with cryopumps. We define the dimensional facility parameters as the background pressure, P_B, effective chamber length, L_{cham}, chamber radius, R_{cham}, chamber surface area, A_{cham}, reference potential in the plume, ϕ_{plume}, atmospheric temperature, T_{atm}, temperature of the shrouds, T_{shrou} , and the surface area of the shrouds that faces the inside of the chamber, A_{shrou} . L_{cham} is the axial distance the beam traverses in the vacuum chamber, and ϕ_{plume} is generally assumed to be 20 V above electrical ground but can be varied experimentally by placing a large, biased electrode in front of the thruster [43]. We note that if we wanted to nondimensionalize an analytical expression for the effective pumping speed of the facility, such as that in Ref. 44, we would need to include the relative locations of each cryopump, the surface area of the cryopumps, and the temperature of the cryopumps. Instead of this detailed analysis, we chose to use the resultant background pressure in the chamber.

For the reference facility parameters, we first define the ingested neutral mass flux, $\Gamma_{ing} = P_B\sqrt{\frac{m_p}{2\pi k_B T_{atm}}}$, as the thermal flux from the static background pressure. Next, we define the reference background neutral density, n_{nB}, and the reference electron density at the lateral walls of the chamber, $n_{e,wall}$ as

$$n_{nB} = \frac{P_B}{k_B T_{atm}},\ n_{e,wall} = n_{e,plume}\exp\left(-\frac{\phi_{plume}}{T_{e,plume}}\right), \tag{12}$$

where $n_{e,plume}$ is the reference electron density in the plume, $T_{e,plume} = \frac{T_{e0}}{10}$ is the reference electron temperature in the cathode plume, and it is assumed that the chamber is at ground potential. To define the reference $n_{e,plume}$, we define $n_{e,exit} = n_{i0}u_{i0}\sqrt{\frac{\pi m_e}{8e}}$, the reference electron density at the cathode exit, where $\sqrt{\frac{8e}{\pi m_e}}$ is the reference electron thermal velocity at the cathode exit. Furthermore, $n_{e,plume} = \frac{n_{e,exit}W_{ch}^2}{D_{ch}^2}$ represents the expansion of the cathode plume. Next, we define the reference resistance of the electron-plume current pathway, $R_{e,plume}$ and of the electron-chamber-wall current pathway, $R_{e,wall}$ as

$$R_{e,plume} = \frac{4m_e\nu_{e,plume}L_{cham}}{e^2 n_{e,plume}\pi D_{ch}^2},\ R_{e,wall} = \frac{m_e\nu_{e,wall}R_{cham}}{e^2 n_{e,wall}\pi\left(R_{cham}L_{cham}+\frac{1}{2}D_{ch}L_{cham}\right)}, \tag{13}$$

where $\nu_{e,wall}$ is the electron collision frequency that impedes electron motion from the cathode to the radial chamber wall and $\nu_{e,plume}$ is the electron collision frequency in the plume. Without loss of generality, we define $\nu_{e,wall} = \nu_{e,plume} = n_{nB}\langle\sigma_{en}u_e\rangle|_{T_{e,plume}}$. Lastly, we can define the power radiated from the thruster, Q_{rad}, and the power radiated from the chamber to the thruster, Q_{cham} as

$$Q_{rad} = \sigma_{SB}\varepsilon_R A_R T_w^4,\ Q_{chamb} = \sigma_{SB}\varepsilon_R A_R T_{atm}^4 + \sigma_{SB}\varepsilon_R A_R \frac{A_{shroud}}{A_{cham}}(T_{shroud}^4 - T_{atm}^4) \tag{14}$$

where σ_{SB} is the Stephan-Boltzmann's constant, ε_R is the surface emissivity, A_R is the radiation surface area, we assumed a view factor of 1, and $\frac{A_{shrou}}{A_{cham}}$ represents the relative view factor of the shrouds to the thruster.

For the nondimensional facility effects, we define five fundamental nondimensional parameters in Table 8. F_1-F_3 represent pressure facility effects, F_4 represents electrical facility effects, and F_5 represents thermal facility effects. While F_1-F_5 are the fundamental nondimensional facility effect parameters in terms of physical relevance, we could have separately defined nondimensional facility effect parameters for $\frac{L_{cham}}{L_{ch}}$, $\frac{R_{cham}}{D_{ch}}$, $\frac{T_{atm}}{T_w}$, $\frac{T_{shrou}}{T_w}$, $\frac{A_{shro}}{A_{cham}}$, and $\frac{\phi_{plume}}{T_{e,plume}}$. In addition, while the definition of nondimensional facility effects in terms of characteristic properties should not depend on any assumptions, the definition in terms of facility and discharge parameters does depend on the assumptions we make to define the characteristic properties.

Table 8. Fundamental nondimensional HET facility effect variables are defined in terms of characteristic properties. Using the same assumptions used to define these characteristic properties in Eqs. 12-14, the nondimensional facility effect variables are expressed in terms of the facility and HET parameters.

Nondimensional Variable	Definition in terms characteristic properties	Expression in terms of facility and discharge parameters
F_1	$\frac{\Gamma_{ing}}{neutral\ mass\ flux\ through\ the\ anode}$	$\frac{P_B W_{ch} D_{ch}}{\dot{m}_a}\sqrt{\frac{\pi m_p}{2k_B T_{atm}}}$
F_2	$\frac{n_{nB}}{n_{n0}}$	$\frac{P_B W_{ch} D_{ch}\sqrt{8\pi m_p k_B T_w}}{k_B T_{atm}\dot{m}_a}$
F_3	$\frac{L_{cham}}{\lambda_{CEX,B}}$	$\frac{P_B k_{CEX,0} L_{cham}}{k_B T_{atm}}\sqrt{\frac{m_p}{2eV_d}}$
F_4	$\frac{R_{e,plume}}{R_{e,wall}}$	$4\frac{L_{cham}^2}{D_{ch}^2}\left(1+\frac{D_{ch}}{2R_{cham}}\right)\exp\left(-\frac{\phi_{plume}}{T_{e,plume}}\right)$
F_5	$\frac{Q_{cham}}{Q_{rad}}$	$\left(1-\frac{A_{shroud}}{A_{cham}}\right)\left(\frac{T_{atm}}{T_w}\right)^4 + \frac{A_{shroud}}{A_{cham}}\left(\frac{T_{shroud}}{T_w}\right)^4$

It is also important to note that the form of F_4 in Table 8 depends on our assumptions for $\frac{\nu_{e,plume}}{\nu_{e,wall}}$ and $\frac{T_{e,plume}}{T_{e0}}$. A 0D cathode plume model could be used to obtain an expression for $\frac{T_{e,plume}}{T_{e0}}$ that depends on C_1, C_2, and C_3 in addition to the nondimensional thruster parameters. Similarly, $\frac{\nu_{e,plume}}{\nu_{e,wall}}$ depends on the closure for anomalous transport in the thruster plume, which would also depend on the nondimensional thruster parameters. As a result, such corrections to $\nu_{e,plume}$ and $T_{e,plume}$ can be viewed as nondimensional parameters that are defined by the previously defined

nondimensional facility and thruster parameters. So, if we are only concerned with defining the set of nondimensional parameters that define the nondimensional facility effects, then there is no need to define the corrections to $\frac{\nu_{e,plume}}{\nu_{e,wall}}$ and $\frac{T_{e,plume}}{T_{e0}}$. However, to accurately estimate how $\frac{R_{e,plume}}{R_{e,wall}}$ varies as a function of the dimensional facility and thruster, then we would need to define the corrections to $\frac{\nu_{e,plume}}{\nu_{e,wall}}$ and $\frac{T_{e,plume}}{T_{e0}}$.

D. Physical Relevance of Nondimensional Facility Effects

Using the characteristic HET parameters from Section II and using characteristic facility parameters of $P_B = 10^{-5}$ Torr, $L_{cham} = 5$ m, $R_{cham} = 2$ m, $A_{cham} = 70$ m^2, $\phi_{plume} = 20$ V, $T_{atm} = 295$ K, $T_{shroud} = 100$ K, and $A_{shroud} = 25$ m^2, we find $F_1 = 3.9 \times 10^{-3}$, $F_2 = 0.02$, $F_3 = 1.6$, $F_4 = 13$, and $F_5 = 0.08$. The selected values for the characteristic facility parameters are representative of facilities used to test HETs of around 5 kW. A value of $F_3 = 1.6$ means that around 50% of beam ions undergo a charge-exchange collision before reaching the end of the chamber; while this effect influences raw measurements of Faraday probes [45] and back-sputtering rates in the facility, this effect should not influence thrust measurements because the ions are fully accelerated and charge-exchange collisions do not contribute significantly to the ingested flux from the facility background pressure. A value of $F_4 = 13$ indicates that most electrons reach the laterals wall of the chamber instead of going into the thruster plume; while this value is sensitive to our estimates of ϕ_{plume} and $T_{e,plume}$, the value indicates the significant presence of additional electron neutralization pathways. In addition, the value for F_4 can be manipulated with a biased beam target to achieve space-like conditions, as done in Ref. 43. Next, the value for F_5 indicates that thermal radiation from the chamber surfaces to the thruster plays a small but nonnegligible role in determining the thruster temperature. Lastly, F_1 and F_2 are intended to show the impact of background pressure on thruster performance. However, while F_1 and F_2 may be related to pressure facility effects, their low characteristic values suggest that they are not the most physically relevant parameters.

III. Methodology for Analyzing Pressure Studies

In analyzing data from past pressure studies, our goal is to illustrate how a nondimensional framework can be used to reduce the dimensionality of pressure facility effects. Reducing the dimensionality of pressure facility effects would simplify the experimental characterization of pressure facility effects in a way that could be applicable to all discharge conditions.

Existing pressure studies typically measure how thrust changes with background pressure at either a single or various discharge conditions. To apply the nondimensional framework to this problem, we first must nondimensionalize the thrust. To this end, we will focus on relative changes in thrust with background pressure.

The thrust, T, can be expressed as $T = T_0 f(A_1, \dots, T_1, \dots P_1, \dots, B_1, \dots F_1, \dots)$, where T_0 is an arbitrary reference thrust value, and $f(A_1, \dots, T_1, \dots P_1, \dots, B_1, \dots F_1, \dots)$ is a universal function of all the nondimensional parameters that describe the nondimensional HET discharge and the nondimensional facility effects. When analyzing a pressure study at a single reference discharge condition, we will choose one thrust value, T^0, as the reference value, which can be expressed as $T^0 = T_0 f(A_1^0, \dots, T_1^0, \dots P_1^0, \dots, B_1^0, \dots F_1^0, \dots)$, where the superscript on the nondimensional parameters indicates the value of that nondimensional parameter that corresponds to T^0. Then, for all the other thrust values in the pressure study at the same reference discharge condition with $T = T_0 f(A_1^0, \dots, T_1^0, \dots P_1^0, \dots, B_1^0, \dots F_1, \dots)$, we can define the normalized thrust as

$$T^* = \frac{T}{T^0} = \frac{f(A_1^0,\ldots,T_1^0,\ldots P_1^0,\ldots,B_1^0,\ldots F_1,\ldots)}{f(A_1^0,\ldots,T_1^0,\ldots P_1^0,\ldots,B_1^0,\ldots F_1^0,\ldots)}, \quad (15)$$

where only the nondimensional facility effects have changed between the two conditions. Because $f(A_1,\ldots,T_1,\ldots P_1,\ldots,B_1,\ldots F_1,\ldots)$ is a universal function, $f(A_1^0,\ldots,T_1^0,\ldots P_1^0,\ldots,B_1^0,\ldots F_1^0,\ldots)$ is universal constant, such that T^* is a universal function of $(A_1^0,\ldots,T_1^0,\ldots P_1^0,\ldots,B_1^0,\ldots F_1^0,\ldots)$ and of $(F_1,\ldots)$. To compare T^* across different discharge conditions, we can consider T^* to be a function of $(A_1,\ldots,T_1,\ldots P_1,\ldots,B_1,\ldots F_1,\ldots)$ evaluated at $(F_1^0,\ldots)$. A key point is that because T^* should only be affected by the coupling between the facility and the discharge, certain nondimensional discharge parameters that are important to determine HET performance may not play a role in T^*. A reduced dimensionality would then correspond to a reduction in the number of nondimensional parameters necessary to describe T^*.

A. Reduction in Dimensionality

First, for simplicity, we will focus on comparing pressure studies conducted in the same chamber with the same chamber electrical configuration. In doing so, we ensure constant nondimensional parameters for those that govern electrical facility effects and thermal facility effects. However, the study will miss effects due to facility geometry, electrical facility effects, and thermal facility effects.

To reduce the dimensionality of pressure facility effects, we need to consider the main ways through which background pressure can change thrust. These are an increase in the effective flow rate through ingestion [46], a change in cathode coupling voltage [47, 48], charge-exchange collisions with background neutrals that prevent ions from being completely accelerated, background neutrals contributing significantly to electron transport in the discharge channel. Each of these phenomena should be able to be described by newly defined nondimensional pressure parameters that are functions of the previously defined facility and discharge nondimensional parameters. Consequently, T^* would be a function of just these four newly defined nondimensional parameters, and the dimensionality of T^* would be significantly reduced.

While modeling pressure facility effects is out of the scope of this study, we can preliminarily define new nondimensional pressure parameters. We can then plot existing data against these newly defined nondimensional parameters and see if they are successful in reducing the dimensionality of pressure facility effects. When we plot data from existing pressure studies, if a variable reduces the dimensionality of facility effects, we mean that the different curves of T^* for the different discharge conditions collapse onto one curve.

B. Additional Pressure Parameters

Additional nondimensional pressure parameters that we believe are related to pressure facility effects include but are not restricted to F_6-F_{10}, defined in Table 9. While these new parameters should be related to the effects of cathode coupling, charge-exchange collisions, and electron transport in the discharge channel, we have not yet considered modifications to the ingestion parameter, F_1. Regarding the ingested neutral mass flux, the thermal flux used in Table 8 is not sufficient to explain experimental observations [5, 46]. It has been suggested that the dynamic pressure of the background neutrals dominates the ingested neutral flux [46, 49]. The characteristic neutral velocity for the dynamic pressure depends on whether the neutrals thermally accommodate with the chamber walls. If they do thermally accommodate, then the characteristic velocity is the thermal velocity at the vacuum facility wall, which we will assume to be the atmospheric temperature; the corresponding nondimensional parameter would be proportional to F_1. If neutrals do not thermally accommodate with the chamber walls, then their characteristic velocity should be the ion's

exhaust velocity, u_{i0}. In this case, we can estimate the ingested neutral flux with a dynamic pressure corresponding to the neutral density of n_{nB} with velocity u_{i0}; it turns out that the corresponding nondimensional parameter for this modified ingested flux is proportional to F_7.

Table 9. Auxiliary nondimensional HET facility effect variables are defined in terms of characteristic properties. Using the same assumptions used to define these characteristic properties, the nondimensional facility effect variables are expressed in terms of the fundamental nondimensional facility effect variables and the nondimensional HET variables.

Nondimensional Variable	Definition in terms characteristic properties	Definition in terms of fundamental nondimensional variables
F_6	$\frac{n_{nB}}{neutral\ density\ at\ channel\ exit}$	$F_2 \exp\left(\frac{1}{A_1}\right)$
F_7	$\frac{n_{nB}}{n_{i0}}$	$\frac{F_2}{A_4}$
F_8	$\frac{L_{ch}}{\lambda_{CEX,B}}$	$\frac{F_2 A_4}{A_1 P_9}$
F_9	$\frac{\Gamma_{ing}}{neutral\ mass\ flux\ through\ the\ cathode}$	$\frac{1}{4}\frac{F_1}{C_1 C_3^2 T_2}$
F_{10}	$\frac{n_{nB} k_{en0}}{\omega_{ce0}}$	$\frac{F_2 A_2 \sqrt{P_1}}{A_1 P_7}$

In addition, the ingested flux also depends on the spatial distribution of the dynamic background pressure, which is determined by the locations of the cryopumps and by the location of the sources of neutrals inside the chamber [49]. These locations could be described by the nondimensional parameters. In fact, Ref. 46 defined nondimensional variables of the cryopump configuration to improve the estimate of the ingested neutral flux. However, to avoid having to incorporate such parameters, we will only compare pressure studies done in the same facility, which should maintain a constant spatial distribution of dynamic pressure.

C. General Methodology

If we believe T^* to be a function of just two variables, say F_1 and F_2, then a plot of T^* is defined by the reference values F_1^0 and F_2^0. Then, to compare T^* at two different discharge conditions, one discharge condition must achieve F_1^0 and F_2^0 at a background pressure P_1 and the other discharge condition must achieve F_1^0 and F_2^0 at another background pressure, P_2. If the range of pressures or the selected discharge conditions in the pressure study do not allow for a common set of (F_1^0, F_2^0) between the discharge conditions, then the pressure study cannot be used to evaluate whether T^* is a function of only F_1 and F_2. Consequently, the choice of discharge conditions and range of background pressures requires careful selection to be able to use the nondimensional framework. If such conditions are met, then T^* is in fact a function of only F_1 and F_2 if different discharge conditions and thrusters are shown to have the same T^* function. Conversely, discrepancies between T^* curves would indicate T^* is not a function of only F_1 and F_2.

The use of such a T^* function can be seen in the following case. Consider that the function T^* has been experimentally mapped out, evaluated with F_1^0 and F_2^0 at space conditions. Then, for any new thruster or discharge

condition, once F_1 and F_2 are calculated, T^* could be used to scale the thrust at an elevated background pressure to that in space.

D. Challenges in Implementation

There are four main challenges in applying the general methodology to existing pressure studies. First, existing pressure studies at different discharge conditions do not have setpoints with a common set of nondimensional facility effect parameters. Second, most pressure studies vary the anode mass flow rate to keep a constant discharge current across different background pressures. Third, different mechanisms have been used to achieve elevated background pressures. Fourth, a thruster body temperature that would scale with T_w is rarely reported in pressure studies.

The first challenge is the most significant, as it prevents us from constructing multi-dimensional plots of T^* based on existing data. This occurs for two reasons. First, as previously mentioned, the discharge condition must be carefully varied to ensure that there is a background pressure at which two operating conditions have the same values for each of the relevant nondimensional parameters. Second, it is unclear which set of nondimensional pressure parameters is the most physically relevant. To illustrate the first point, we can consider two cases. For the case of two discharge conditions with different $\dot{m}_a$, $\dot{m}_1$ and $\dot{m}_2$, then we can match F_3 if they were operated at the same background pressure, but at that same background pressure, the values for F_1 would be off by a factor of $\frac{\dot{m}_1}{\dot{m}_2}$. Similarly, for the case of two discharge conditions with different V_d, V_1 and V_2, we can match F_1 if they were operated at the same background pressure, but at that same background pressure, the values for F_7 would be off by a factor of $\sqrt{\frac{V_1}{V_2}}$.

Regarding the second challenge, by changing $\dot{m}_a$ at each pressure, the values for A_1 are different at each pressure. In fact, in Ref. 5, $\dot{m}_a$ varied by as much as 10% between the discharge conditions. Calculating each T^* curve with Eq. 15 assumes that each point along that curve has the same nondimensional discharge condition, so a different A_1 at each pressure would not allow using the nondimensional framework to analyze such data. Because of this, we will mostly consider pressure studies that either purposefully maintained a constant $\dot{m}_a$ or where $\dot{m}_a$ varied by less than 1% across the various pressures.

We do acknowledge that pressure studies at constant discharge current are useful for flight qualification testing, especially in the case of HETs with a center-mounted cathode, which have shown to have an approximately constant thrust at various pressures [3, 4, 6]. However, to isolate the effects of nondimensional facility effects on the discharge, it is better to keep $\dot{m}_a$ constant so that all the nondimensional discharge parameters are constant. It would be possible to define an effective $\dot{m}_a$ based on an approximation for the ingested flow rate, but it is known that ingested neutrals do not undergo the same processes as neutrals injected through the anode.

As for the third challenge, the mechanism by which a study achieves an elevated background pressure can affect the spatial distribution of the static and dynamic background pressure. If this spatial distribution varies significantly across each pressure, then we would need to account for the nondimensional parameters that govern the spatial distribution of the dynamic background pressure. The three mechanisms used to increase the background pressure are reducing the number of active cryopumps, injecting excess propellant from somewhere in the chamber, and a combination of the previous two methods. From the model in Ref. 46, if the number of active cryopumps is reduced, this should change the ratio of the dynamic pressure to the static background, but we are not aware of this effect being quantified. In addition, when injecting extra propellant to increase the background pressure, it is possible that the ratio of the flow rate of the excess neutrals to the anode flow rate affects the spatial distribution of the dynamic pressure, but we are also not aware of this effect being quantified. So, although we believe the mechanism used to achieve an

elevated background pressure may affect the ratio of ingested flux to the thermal flux, this effect has not been quantified. As a result, we will consider pressure studies, independent of which mechanism was used.

Lastly, regarding the fourth challenge of the implementation, because a reference temperature that scales with T_w is typically not reported, rough estimates are needed to approximate how $\frac{T_w}{T_{atm}}$ scales with the operating condition. Such estimates for $\frac{T_w}{T_{atm}}$ are necessary to accurately estimate how F_2 changes between discharge conditions. In the range of discharge conditions that we will consider, accounting for a changing T_w has a negligible effect on our analysis. However, variations in $\frac{T_w}{T_{atm}}$ are important because $F_2 \sim F_1\sqrt{\frac{T_w}{T_{atm}}}$, so if we to assume that T_w is independent of the discharge condition and that T_{atm} is constant, then F_1 and F_2 would no longer be independent parameters.

E. Revised Methodology

To address the first challenge, we had to implement the following simplified analysis. We consider the various nondimensional pressure parameters separately. We then assume that T^* is a function of only one of these nondimensional parameters and plot T^* against that nondimensional pressure parameter. We will then compare the different plots to see if one nondimensional parameter is able to successfully reduce the dimensionality of the T^* curves at different discharge conditions. In addition, to be able to find common values for all the nondimensional pressure parameters among the different discharge conditions, we need to interpolate between the reported thrust values. The interpolation is done by assuming that the plot of thrust vs. P_B is of the form $T = A - B\exp(-CP_B)$.

Next, to address the second challenge, because there are so many existing pressure studies that were done at constant discharge current, it is useful to consider how we can approximately correct for a varying $\dot{m}_a$. We would start by constructing the T^* as if $\dot{m}_a$ was constant. Denoting the mass flow rate at the reference condition as $\dot{m}_a^0$ and if we assume that the thrust scales approximately with $\dot{m}_a$ within a small range of $\dot{m}_a$, then the value of T^* at $\dot{m}_a$ should be scaled by $\frac{\dot{m}_a^0}{\dot{m}_a}$. Also, if we are plotting T^* as a function of $\frac{P_B}{\dot{m}_a}$ for different $\dot{m}_a^0$, then we should actually plot $T^*\frac{\dot{m}_a^0}{\dot{m}_a}$ as a function of $\frac{P_B}{\dot{m}_a^0}$.

The first set of pressure studies we considered was the measurements in Ref. 1, which were done at various mass flow rates and magnetic field strengths. Specifically, in Ref. 1, the discharge voltage was 300 V, the discharge current was varied between 3 A and 15 A, and the background pressures were between 1 and 14 μTorr-Xe. We chose to only analyze the conditions between 2.5 and 4.5 kW because, even though the pressure studies at each discharge power were done at constant discharge current, at discharge powers between 2.5 and 4.5 kW, the change in mass flow rate at different pressures was around 1%. We will construct two plots, one of T^* as a function of F_2 and one of T^* as a function of F_6. These measurements were made on the SPT-140, and we estimate $A_1 = 0.19$ at 300 V and 15 A on the SPT-140. The values for A_1 at the other anode flow rates can then be scaled according to the expression for A_1 in Table 6.

To illustrate how the F_2^0 and F_6^0 values are selected for the SPT-140 data, we refer to Figs. 2 and 3. The range of F_2^0 values that we can select from are those at which there is a corresponding thrust value for all the discharge conditions; in Fig. 2, this results in a possible range of F_2^0 values approximately between 0.004 and 0.035. While there is no exact criterion for selecting F_2^0 and F_6^0 values, a rule of thumb should be to select values such that most of the curves have a balanced number of values on either side of F_2^0 and F_6^0. For example, in Fig. 2, the selected value of F_2^0 results in the 2.5 kW and 4.5 kW cases having the most unbalanced numbers of values on either side of F_2^0, with both

cases having 3 values to the right of F_2^0 and 6 values to the left of F_2^0. On the other hand, Fig. 3 shows that it is difficult to select an ideal F_6^0 for the available data, as the unbalanced number of values on either side of F_6^0 for the 2.5 kW and 4.5 kW cases are unavoidable if both cases are considered simultaneously.

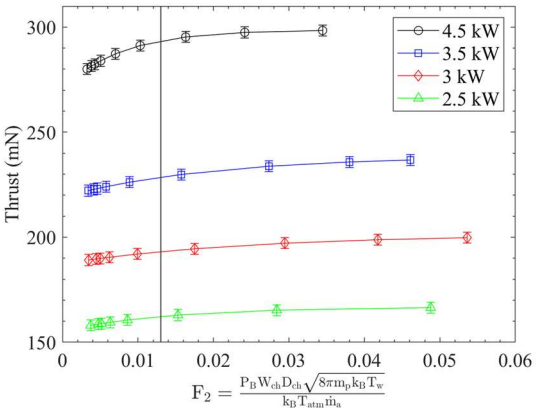

Figure 2. Thrust versus $F_2 = \frac{P_B W_{ch} D_{ch} \sqrt{8\pi m_p k_B T_w}}{k_B T_{atm} \dot{m}_a}$ at different anode flow rates at constant discharge voltage, corresponding to four different discharge powers. The vertical line is at the selected value of $F_2^0 = 0.013$. Data adapted from Ref. 1.

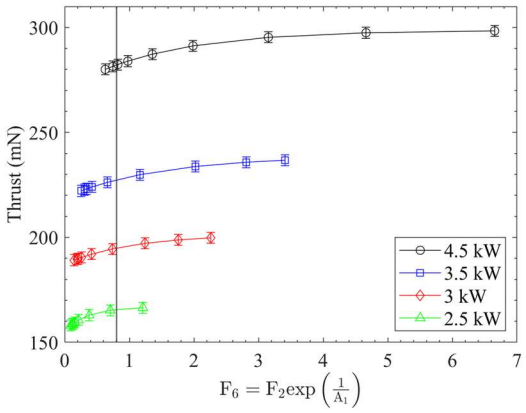

Figure 3. Thrust versus $F_6 = F_2 \exp\left(\frac{1}{A_1}\right)$ at different anode flow rates at constant discharge voltage, corresponding to four different discharge powers. The vertical line is at the selected value of $F_6^0 = 0.8$. Data adapted from Ref. 1.

The second set of pressure studies we considered was the measurements in Ref. 2, which were done at various discharge voltages and anode flow rates. Specifically, in Ref. 2, the discharge voltage was varied between 300 V and 600 V, the anode mass flow rate was either 5.25 mg/s or 10.46 mg/s, and the background pressures were between 5 and 14 μTorr-Xe. To isolate the effect of the discharge voltage on T^*, we will only consider the data at the low flow rate and on the P5-A thruster. This data was obtained with a constant anode flow rate across the various background pressures and discharge voltages. To analyze this data with the nondimensional framework, we will construct two plots, one of T^* as a function of F_2 and one of T^* as a function of F_7. The plots used to select F_2^0 and F_7^0 are shown in Figs. 4 and 5.

The last set of pressure studies we considered was the measurements in Ref. 3, which were done at various cathode flow fractions, C_1. Specifically, we will analyze the data in Ref. 3 that was done with an externally mounted cathode, at a discharge voltage of 300 V, discharge current of 15 A, and background pressure between 5 and 20 μTorr-Xe. To analyze this data with the nondimensional framework, we will construct two plots, one of T^* as a function of F_2 and one of T^* as a function of F_9. However, the discharge current was kept constant in this study, and the anode flow rate at each pressure was not reported. To correct for the change in $\dot{m}_a$ and $\dot{m}_c$, we use the results in Ref. 4 conducted on a similar HET and discharge condition and with an externally mounted cathode. They found a reduction in $\dot{m}_a$ with increased background pressure at a rate of approximately $\frac{1}{50} \frac{mg/s}{\mu Torr-Xe}$. We then assume that Ref. 3 operated the H9 at 15 mg/s to achieve 15 A on xenon. With these assumptions, we can approximately correct T^* and F_9. The plots used to select F_2^0 and F_9^0 are shown in Figs. 6 and 7.

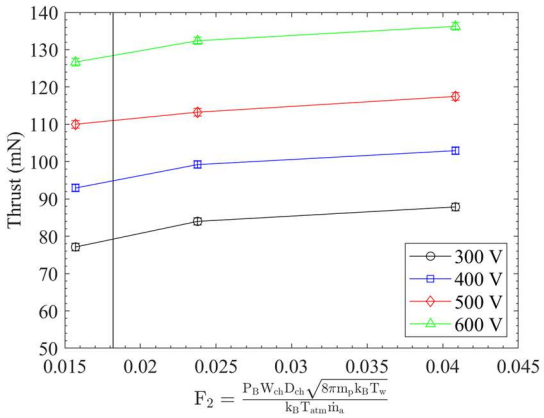

Figure 4. Thrust versus $F_2 = \frac{P_B W_{ch} D_{ch} \sqrt{8\pi m_p k_B T_w}}{k_B T_{atm} \dot{m}_a}$ at different discharge voltages at constant flow rate. The vertical line is at the selected value of $F_2^0 = 0.0182$. Data adapted from Ref. 2.

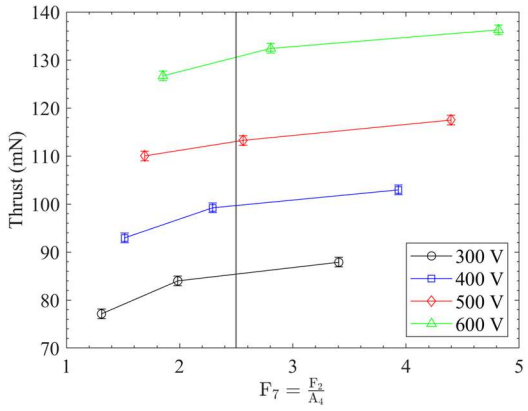

Figure 5. Thrust versus $F_7 = \frac{F_2}{A_4}$ at different discharge voltages at constant flow rate. The vertical line is at the selected value of $F_7^0 = 2.5$. Data adapted from Ref. 2.

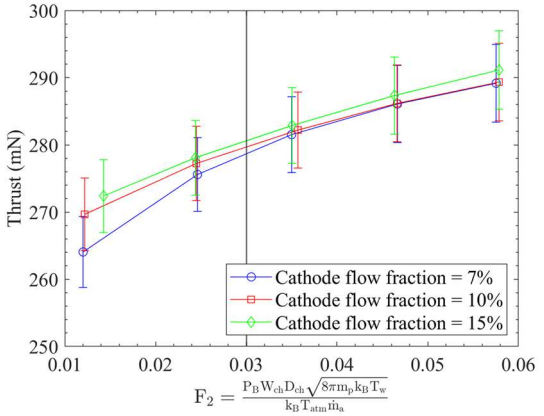

Figure 6. Thrust versus $F_2 = \frac{P_B W_{ch} D_{ch} \sqrt{8\pi m_p k_B T_w}}{k_B T_{atm} \dot{m}_a}$ at different cathode flow fractions. The vertical line is at the selected value of $F_2^0 = 0.03$. Data adapted from Ref. 3.

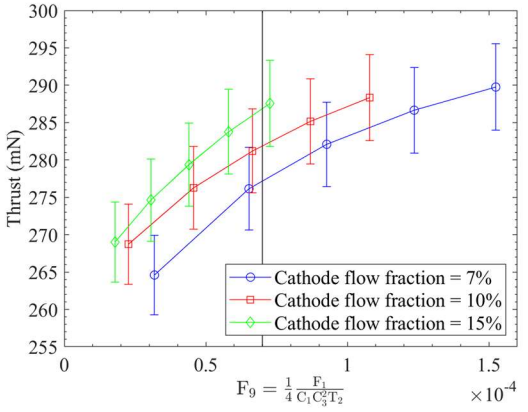

Figure 7. Thrust versus $F_9 = \frac{1}{4} \frac{F_1}{C_1 C_3^2 T_2}$ at different cathode flow fractions. The vertical line is at the selected value of $F_9^0 = 7 \times 10^{-5}$. Data adapted from Ref. 3.

Regarding the uncertainty, for the thrust measurements in Ref. 1, we assumed an uncertainty of ± 2.6 mN, for the thrust measurements in Ref. 2, we assumed an uncertainty of ± 1 mN, and for the thrust measurements in Ref. 3, we assumed an uncertainty of $\pm 2\%$. Next, to quantify the uncertainty in T^*, we used a simplified approach. Once the reference value for say F_2^0 is selected, the corresponding T^0 value is found via interpolation. We assume no uncertainty

in the T^0 value but then include the above uncertainties in the thrust values when calculating $T^* = \frac{T}{T^0}$. In this manner, our reported uncertainty in T^* is a lower bound for the uncertainty.

IV. Similarity of HET Discharges

We can consider the nondimensional discharge to be defined by the discharge condition (A_1, A_2, A_3, A_4, and C_1), the propellant (P_1, P_2, and P_8), thruster geometry (T_1, T_2, and C_2), thruster material (T_3), and magnetic field topology (A_9-A_{12}). Even in the case where non-Maxwellian effects and the induced magnetic field are non-negligible, A_5, A_6, and A_7 are not necessary to define the discharge. This is because a given set of A_1, A_2, A_3, A_4, T_1, and T_2 is defined by a single set of $\frac{\dot{m}_a}{W_{ch}D_{ch}}$, V_d, B_{r0}, T_w, L_{ch}, W_{ch}, D_{ch}, and the propellant, which also fully defines A_5, A_6, and A_7. In addition, A_8 is defined by the nondimensional magnetic field topology, A_9-A_{12}.

In this section, we will consider which HET operating conditions and designs can be considered dynamically similar. That is, are there different combinations of $\dot{m}_a$, V_d, B_{r0}, T_w, L_{ch}, W_{ch}, and D_{ch} that produce the same A_1, A_2, A_3, A_4, T_1, and T_2? This would be very useful for the scaling of HETs between discharge conditions and between sizes, as dynamically similar discharges should have the same efficiencies and nondimensional plasma properties. In addition, if two thrusters of different sizes are exactly similar, then the smaller thruster could be tested at lower background pressures than the larger thruster. So, while exact similarity would be greatly beneficial to HET scaling, it can also be useful for the study of pressure facility effects. We note that the inclusion of A_3 in developing similarity laws is a novel approach, which allows a similarity-based scaling of $\dot{m}_a$, V_d, and B_{r0}, which previously required an additional constraint like current density. However, an important caveat the similarity laws developed in this section use the definitions in Table 6, which assume $\frac{n_{e0}}{n_{i0}} = \frac{u_{ez}}{u_{i0}} = \frac{10T_{e0}}{V_d} = 1$, such that the presented similarity laws could be made more accurate in future work with the combination of 0D electron model of the HET discharge.

We will first present similarity laws for exact dynamic similarity between different thruster geometries. We will then develop similarity laws for approximate dynamic similarity of different discharge conditions ($\frac{\dot{m}_a}{W_{ch}D_{ch}}$, V_d, B_{r0}, and T_w) on different thrusters. Lastly, we will develop similarity laws for approximate dynamic similarity between discharge conditions with different propellants on the same thruster and on different thrusters. Each similarity law we present assumes that a certain set of nondimensional parameters are the only ones that govern HET performance. For alternative HET designs, new nondimensional parameters may need to be defined and may significantly impact HET performance, and at significantly different operating conditions, different nondimensional parameters may become more or less important. Consequently, the presented similarity laws likely do not apply across HET designs that require different amounts of nondimensional parameters or across significantly different operating conditions.

Before proceeding, it is important to clarify the difference between exact similarity and approximate similarity. The first cause of approximate similarity is that HETs typically do not control T_w, so we will not consider T_w a controllable discharge condition. Because T_w is not controllable, in most situations, we will need to pick one of A_1, A_2, A_3, and A_4 to not keep constant. We believe that A_4 should be the least significant among the four, so we define one case of approximate similarity to be when A_1, A_2, and A_3 are constant and A_4 is not constant. When A_4 is not held constant, approximate similarity will not ensure that A_5, A_6, and A_7 are constant.

In addition, because some HETs cool the channel walls [50] and most do not cool the channel walls, we will keep the scaling relations in terms of T_w. In this manner, the presented relations are valid for all thermal designs of HETs. Furthermore, whenever T_{e0} changes, this introduces approximate similarity due to the nonlinearity of ionization rates

of neutrals and of ions. First, as shown in Fig. 8, the nondimensional function of the ionization rate of neutrals, k_{iz}^*, depends on the choice of T_{e0}. As T_{e0} increases, k_{iz}^* at temperatures less than T_{e0} ($T_e^* < 1$) increases. As a result, even if the axial profile of T_e^* is the same across different conditions, the axial profiles of k_{iz1}^* will be different. The exact effect that this would have on the validity of dynamic similarity is unclear, but the nonlinearity of k_{iz1}^* has another important consequence; because k_{iz}^* is nonlinear, the functional form of T_{e0} influences the scaling relations whenever k_{iz} is involved. For example, if $T_{e0} = \frac{V_d}{10}$, then the relative increase of k_{iz} at different voltages will be different compared to if $T_{e0} = \frac{V_d}{20}$. Because a higher fidelity approximation for T_{e0} is out of the scope of this work, whenever k_{iz0} is involved in the scaling relations, we leave the equations in terms of k_{iz0}. Another important consequence of the nonlinearity of k_{iz}^* is that exact dynamic similarity is only possible if the propellant and nondimensional spatial distributions of all dimensional plasma properties are kept constant. Interestingly, if such exact dynamic similarity is possible, it would also ensure constant erosion rates across different conditions.

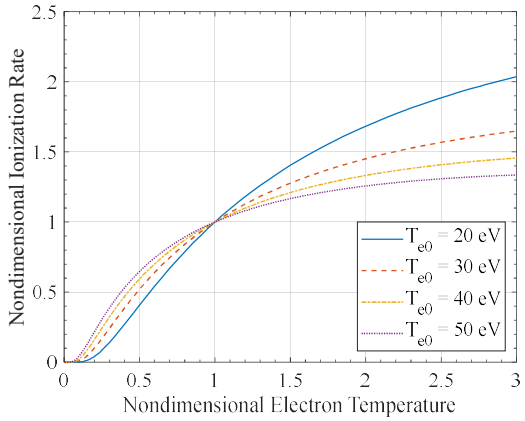

Figure 8. Nondimensional ionization rate of xenon atom, k_{iz1}^*, as a function of nondimensional electron temperature, T_e^* for various T_{e0}.

A. Exact Similarity between Thruster Geometries

To keep a constant nondimensional spatial distribution of dimensional plasma properties to achieve exact dynamic similarity, $\frac{\dot{m}_a}{W_{ch}D_{ch}}$, V_d, B_{r0}, and T_w must be kept constant. It is then not a coincidence that HETs of different sizes tend to have similar $\frac{\dot{m}_a}{W_{ch}D_{ch}}$, V_d, and B_{r0}. The question is then, as $\dot{m}_a$ changes, how should the thruster geometry change to ensure exact dynamic similarity? From the constraint of A_2, L_{ch} must be constant to achieve dynamic similarity. From the aspect ratio constraints, then W_{ch} and D_{ch} must also be constant, such that if T_1 and T_2 are both considered important, then two different HETs cannot be exactly similar.

However, HETs can achieve similar scaling (constant A_1, A_2, A_3, A_4, and T_2 and constant $\frac{\dot{m}_a}{W_{ch}D_{ch}}$, V_d, B_{r0}, and T_w) according to Eq. 16 with a constant L_{ch} and nondimensional magnetic field topology if wall effects are negligible. Equation 16 implies that HETs with negligible wall effects can scale in size at constant current density and thrust density. What may seem like a caveat to the scalability of HETs with negligible wall effects is that as they scale up in

size, $T_1 \equiv \frac{L_{ch}}{W_{ch}}$ would decrease. On its own, a decreasing T_1 would influence the divergence efficiency through the nondimensional radial electron momentum equation, Eq. 10. However, to keep a constant nondimensional magnetic field, $A_8 T_1 T_2$ must be constant. Therefore, with a constant T_2, $A_8 T_1$ will be constant in Eq. 10. As a more general result, nondimensional radial effects are constant at different T_1 if T_2 and the nondimensional magnetic field are constant.

$$\dot{m}_a \sim \sqrt{W_{ch}},\ D_{ch} \sim W_{ch}. \tag{16}$$

To understand when wall effects become negligible for annular HETs we can consider the nondimensional fluid equations. In the continuity equations, as A_1 approaches zero, any ion that recombines at the wall will immediately be ionized, such that wall recombination has a negligible effect on the continuity equations. Thus, wall effects should not affect the mass utilization efficiency as A_1 approaches zero. However, it should be considered that as A_1 approaches zero, n_n^* should also approach zero, which may reduce the dominance of neutral ionization in the neutral continuity equation. In addition, in the electron energy equation, as A_1 approaches zero, electron energy losses due to ionization will be the dominant form of electron energy losses, such that wall losses will have a negligible effect on the electron energy dynamics. In the case of the energy dynamics, as n_n^* goes to zero, the ionization losses from the ionization of ions will be the dominant energy loss mechanism. In terms of the energy efficiency, as A_1 approaches zero, inelastic losses should dominate over wall losses, such that wall effects have a negligible influence on the energy efficiency. In general, as A_1 approaches zero, collisional effects are expected to dominate over wall effects.

In terms of discharge parameters, $A_1 \sim \frac{A_{ch} W_{ch} \sqrt{V_d}}{\dot{m}_a k_{iz,0}}$, such that A_1 approaches zero for large $\frac{\dot{m}_a}{W_{ch} D_{ch}}$. While we are not able to say at what point wall effects become negligible with increasing current density, we can qualitatively state that as current density increases, wall effects should eventually have a decreased effect on the discharge, even though the heat load on the channel walls increases. This is an interesting finding, as high current density operation of HETs has received recent attention [50].

However, at high current densities the induced magnetic field should be non-negligible. Since the induced magnetic field is mostly generated by the Hall current, it can be approximated as the magnetic field produced by a finite-length solenoid. By changing T_1, we would effectively be changing the aspect ratio of the finite solenoid, which should change the nondimensional induced magnetic field. Whether these end effects would have a significant effect on the discharge is unclear, but it may be something to consider when scaling high current density HETs. Lastly, because of the finite curvature in the magnetic field, when the shape of nondimensional magnetic field lines is kept constant by keeping $A_8 T_1 T_2$ constant, there is an avoidable change in the nondimensional shape of the lines perpendicular to the magnetic field lines. Once again, while the effect of this on the discharge is unclear, its effect should be considered when using the scaling suggested by Eq. 16. Nevertheless, if Eq. 16 with constant L_{ch} is used to scale HETs to higher powers, the increase in T_1 should reduce wall losses. As a result, lower power HETs could provide a lower bound for efficiency of higher power HET if Eq. 16 is used for scaling.

B. Comparison with Empirical Scaling

Empirical scaling laws indicate $W_{ch} \sim D_{ch}$ [51]. In addition, HETs generally operate in similar ranges of V_d, B_{r0}, and $\frac{\dot{m}_a}{W_{ch} D_{ch}}$. This results in a scaling similar to Eq. 16, but L_{ch} is strongly correlated to W_{ch} and D_{ch} in empirical data [51].

These relationships result in A_1 and A_2 decreasing at higher powers while keeping A_3 constant. So, while the scaling does not produce similar thrusters, it has been suggested that as long as A_1 is below 1/3, the thruster should be efficient [16], so a decrease in A_1 may be desirable; this is because a lower A_1 corresponds to a higher mass utilization. The empirical scaling suggests that a similar criterion may exist for A_2, which is already much less than 1 in typical operating conditions. Consequently, while empirical HET scaling may not satisfy similarity, higher powers thrusters should see improved performance, which is observed [52]. These points highlight that traditional HET scaling is not as useful for scaling to low powers.

C. Approximate Similarity Between Discharge Conditions

Regarding whether two discharge conditions on the same thruster (same T_1, and T_2) can be dynamically similar, it is immediately clear that if three nondimensional parameters are important, then if one of $\dot{m}_a$, V_d, or B_{r0}, is changed, then we are left with a system of three equations and two unknowns to determine how the other two parameters should change in response. However, if we can change the thruster size while retaining geometric similarity (T_1 and T_2), then three nondimensional parameters are needed to determine how $\dot{m}_a$, V_d, and B_{r0} should change to retain approximate similarity. If we keep A_1, A_2, A_3, T_1, and T_2 constant, then for a given change in the size of the thruster,

$$\dot{m}_a \sim \left(\frac{L_{ch}}{k_{iz0}}\right)^{3/2} T_w^{3/4},\ B_{r0} \sim \frac{T_w^{1/4}}{\sqrt{L_{ch} k_{iz0}}},\ V_d \sim \frac{L_{ch}\sqrt{T_w}}{k_{iz0}}, \tag{17}$$

where $W_{ch} \sim D_{ch} \sim L_{ch}$. The scaling relations in Eq. 17 are plotted in Fig. 9, assuming a T_w that scales according to the thermal model in the appendix. At the reference condition for plotting Fig. 9, the thermal model predicts $T_w = 692\ K$ when $\varepsilon_R = 0.3$ and $F = 1$. Throughout this section, the relative ratio of a parameter is with respect to the reference condition; for example, if the reference condition has a channel length of L and another condition has channel length of $2L$, then the relative ratio of the channel length for this other condition is 2. The ionization rates of xenon are calculated using the cross-sections from Ref. 53 and assuming a Maxwellian electron speed distribution at an electron temperature of $\frac{V_d}{10}$. Figure 9 covers a factor of 100 in discharge power and shows the magnetic field strength should decrease with thruster size while the voltage should increase with thruster size. In addition, Fig. 9 shows that $\frac{\dot{m}_a}{W_{ch} D_{ch}}$ decreases as thruster size increases, suggesting that larger thrusters should operate at lower current densities. The higher current density and significantly higher magnetic field strengths required for similarity on smaller thrusters may introduce some practical challenges in implementing the scaling relations of Eq. 17. However, the possibility of scaling to smaller thrusters is notable, even if its implementation is not straightforward. In addition, for a tenfold increase in jet power ($\sim \frac{\dot{m}_a V_d}{m_p}$), the relative ratio in thrust density ($\sim \frac{\dot{m}_a}{(W_{ch}+D_{ch})^2}\sqrt{\frac{V_d}{m_p}}$) from Eq. 17 is 0.35. Lastly, at the significantly increased current density for scaling to smaller thrusters suggested by Fig. 9, A_7 may become non-negligible, which would invalidate the similarity law given by Eq. 17.

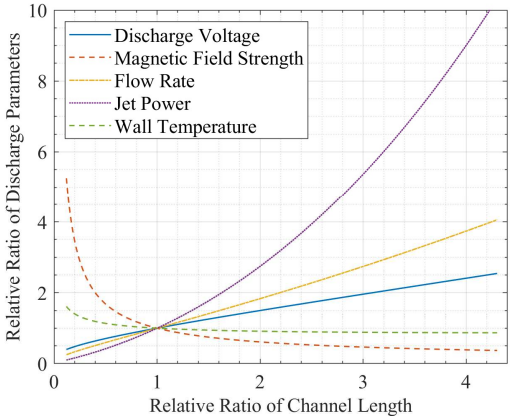

Figure 9. Relative ratio in discharge parameters required for constant A_1, A_2, A_3, T_1, and T_2 as a function of channel length. Reference condition is xenon at 300 V, $\frac{\dot{m}_a}{\pi W_{ch} D_{ch}} = 10^{-3}\,\frac{kg}{s \cdot m^2}$, $L_{ch} = 30\,mm$, $W_{ch} = 30\,mm$, $D_{ch} = 100$, and $\sigma_{SEE} = 0.5$.

D. Approximate Similarity between Propellants

Regarding the dynamic similarity of HET discharges of different propellants, we expect exact dynamic similarity to be impossible because of the importance that P_1 is expected to have on anomalous transport and because of the nonlinearity of the ionization rates. It is also impossible to keep both A_1 and $A_1 P_2$ constant, so a change in P_2 will influence the electron energy dynamics. As such, it may prove that different propellants have different optimal values of A_1, A_2, and A_3 or even of thruster aspect ratios. However, it may still be useful to analyze the scaling relations suggested by nondimensionalization. For similarity between propellants on the same thruster, three nondimensional parameters need to be used to define how $\dot{m}_a$, V_d, and B_{r0} should be changed with propellant, while for similarity between propellants on two geometrically similar thrusters, four nondimensional parameters (or three and one additional constraint) are needed to determine how $\dot{m}_a$, V_d, B_{r0}, and L_{ch} should change.

For different propellants, HET discharges on the same thruster are approximately similar (constant A_1, A_2, and A_3) if

$$\dot{m}_a \sim \frac{T_w^{3/4}}{k_{iz0}^{3/2} m_p^{1/4}}, \; B_{r0} \sim \left(\frac{T_w}{k_{iz0}^2 m_p}\right)^{1/4}, \; V_d \sim \left(\frac{T_w}{k_{iz0}^2 m_p}\right)^{1/2}, \tag{18}$$

Table 10 shows the scaling relations of Eq. 18 applied to krypton and argon assuming a T_w that scales according to the thermal model in the appendix, with $\frac{\dot{m}_a}{m_p}$ being an approximation for the relative increase in discharge current. In Table 10, the reference condition has a thruster wall temperature of 692 K. The ionization rates for krypton and argon were calculated with the cross-sections form Ref. 53. Table 10 suggests that lighter noble gas propellants should be operated at a higher current density, discharge voltage, and magnetic field strength to achieve similar discharge conditions as heavier noble gas propellants. In addition, in terms of thrust ($\dot{m}_a \sqrt{\frac{V_d}{m_p}}$) when using Eq. 18, krypton would have a relative ratio of 2.40 and argon would have a relative ratio of 8.22. Experiments typically observe that lighter propellants achieve less thrust, but it is important to note that these experiments do not conserve nondimensional

parameters when the HET operates with different propellants. The lower ionization rate and higher T_w for lighter propellants requires a significant increase in mass flow rate to maintain a constant A_1, which results in an increased thrust for lighter propellants.

While similar operation between molecular and atomic propellants is unlikely because of the possibility of dissociation, the scaling relations suggested by Eq. 18 may still be useful for molecular propellants. Also, this analysis does not account for the possible effects of non-negligible ion magnetization on lighter propellants, but it may become important to consider as Eq. 18 suggests a stronger magnetic field for lighter propellants. For example, one way to account for ion magnetization is to keep A_1, $\frac{A_2}{\sqrt{P_1}}$, and A_3 constant between propellants since $\frac{A_2}{\sqrt{P_1}}$ corresponds to the degree of ion magnetization. In addition, A_7 may become non-negligible for lighter propellants because of the higher current densities required for similarity. Lastly, the high T_w for lighter propellants indicates that thermal management techniques are necessary to apply the similarity law of Eq. 18 to lighter propellants.

Another useful consideration is how to scale the HET size to achieve approximately similar operation on different propellants at the same current density; this will require adding another constraint in addition to three nondimensional parameters. We choose to also keep A_4 constant due to its presence in the nondimensional fluid equations. The resultant scaling to keep A_1, A_2, A_3, A_4, T_1, and T_2 constant is

$$\dot{m}_a \sim \sqrt{m_p} T_w^{3/2}\ ,\ B_0 \sim \frac{1}{k_{iz1,0}\sqrt{m_p}}\ , V_d \sim T_w,\ L_{ch} \sim k_{iz1,0}\sqrt{m_p T_w}, \tag{19}$$

and $D_{ch} \sim W_{ch} \sim L_{ch}$. Table 11 presents the scaling relations in Eq. 19 for krypton and argon assuming a T_w that scales according to the thermal model in the appendix. This scaling indicates that even after redesigning a HET for different propellants, the discharge voltage, magnetic field strength, current density, and wall temperature all increase for lighter noble gas propellants. Regarding thrust density, krypton has a relative ratio of 2.75, and argon has a relative ratio of 10.19.

Compared to the scaling for propellants on the same thruster, for a redesigned thruster on lighter propellants, the change in discharge voltage decreases, the change in magnetic field strength increases, the current density increases, and the wall temperature increases. As with the results of Table 10, Table 11 also indicates that thermal management techniques are necessary to apply Eq. 19 to lighter propellants. In addition, while the increased magnetic field on smaller HETs may be difficult to implement, the higher voltages on the same thruster required for lighter propellants may pose its own practical challenges. As a result, it is not immediately obvious whether it is more practical to redesign a HET for different propellants or to simply operate different propellants on the same thruster at conditions that satisfy Eq. 18. Lastly, we reiterate the caveat that the conclusions from Eq. 18 and 19 assume that the optimal set of values for the nondimensional parameters is the same across different propellants.

Table 10. Relative ratio in discharge parameters required for constant A_1, A_2, A_3, T_1, and T_2 for different propellants on the same thruster. Reference condition is the same as in Fig. 9.

Propellant	V_d	B_{r0}	$\frac{\dot{m}_a}{m_p}$	T_w
Kr	1.55	1.24	2.42	1.37
Ar	2.87	1.69	8.81	2.19

Table 11. Relative ratio in discharge parameters and channel length required for constant A_1, A_2, A_3, A_4, T_1, and T_2 for different propellants. Reference condition is same as in Fig. 9.

Propellant	V_d	B_{r0}	$\frac{\dot{m}_a}{m_p W_{ch} D_{ch}}$	T_w	L_{ch}
Kr	1.40	1.40	2.91	1.40	0.85
Ar	2.24	2.13	12.35	2.24	0.70

V. Nondimensional Analysis of Existing Pressure Studies

In this section, we present our nondimensionalization of the results of existing pressure studies [1, 2, 3]. We will find that certain nondimensional pressure parameters provide a better description of the normalized data. By construction, in all the plots presented in this section, the different curves of T^* overlap with $T^* = 1$ at the reference value of the nondimensional pressure parameter; this is not an indication of universality, and instead, the different curves should be compared at values away from the reference values of the nondimensional parameters.

In Figs. 10 and 11, the various curves of T^* diverge at values $T^* > 1$, but when T^* is plotted against F_6 in Fig. 11, the curves align to within measurement uncertainty at values $T^* < 1$. On the other hand, when T^* is plotted against F_2 in Fig. 10, the values of T^* for 4.5 kW, diverge outside the uncertainty bounds for $T^* < 1$. In addition, because of the constant discharge voltage and cathode flow fraction among the discharge conditions in Figs. 10 and 11, F_2 is proportional to F_1, F_7, and F_9. Because F_6 makes the different curves of T^* align more closely at low pressures, we can conclude that F_6 is more closely related to the dependence of T^* on the anode flow rate than F_1, F_2, F_7, and F_9. As a result, F_6 may be useful to reduce the dimensionality of pressure facility effects.

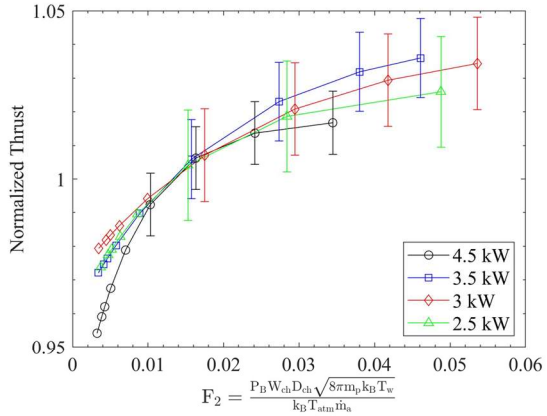

Figure 10. Normalized thrust versus $F_2 = \frac{P_B W_{ch} D_{ch} \sqrt{8\pi m_p k_B T_w}}{k_B T_{atm} \dot{m}_a}$ evaluated at $F_2^0 = 0.013$ for different anode flow rates at constant discharge voltage, corresponding to four different discharge powers. Background pressures vary from 1 to 14 μTorr-Xe. For readability, certain error bars are omitted. Data adapted from Ref. 1.

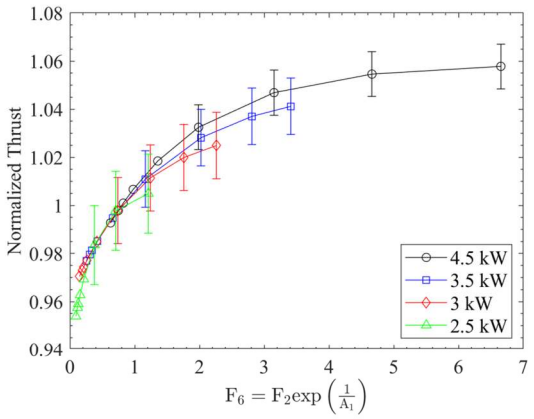

Figure 11. Normalized thrust versus $F_6 = F_2 \exp\left(\frac{1}{A_1}\right)$ evaluated at $F_6^0 = 0.8$ for different anode flow rates at constant discharge voltage, corresponding to four different discharge powers. Background pressures vary from 1 to 14 μTorr-Xe. For readability, certain error bars are omitted. Data adapted from Ref. 1.

The relevance of F_6 can be explained by the fact that F_6 accounts for greater mass utilization at higher flow rates. At a fixed effective pumping speed of the facility, this would increase the ratio of background neutral density to neutral density near the channel exit. Meanwhile, at a fixed effective pumping of the facility F_1, F_2, F_7, and F_9 are constant for a change in anode flow rate, so it is not surprising that these parameters do not accurately capture the effect of anode flow rate on T^*.

However, although the divergence at $T^* > 1$ is within the measurement uncertainty, Fig. 11 seems to indicate that F_6 does not completely describe T^* for large values of F_6. One possible reason for this is that, at the highest pressures in Ref. 1, $F_8 \approx 0.025$, indicating that at high background pressures, charge exchange collisions with background neutrals can prevent a few percent of ions from being fully accelerated. Because F_8 should eventually become important at high pressures and F_6 is important at low pressures, the dimensionality of pressure facility effects increases at high background pressures. Additionally, while the ranges of F_2 values between the different discharge powers are comparable in Fig. 10, Fig. 11 has a reduced range of F_6 values for the lower discharge powers. To more thoroughly study the divergence of at $T^*(F_6) > 1$, future pressure studies done at various anode flow rates should accordingly increase the maximum background pressure for the lower anode flow rate cases.

Figure 12 shows that all the curves at different voltages align within measurement uncertainty, except for at 500 V at the lowest pressure. This indicates that F_7 is closely related to the dependence of T^* on the discharge voltage. However, because F_7 is proportional to F_{11}, the physical explanation for the importance of F_7 is ambiguous. F_7 may seem important because it captures the increase of $\frac{n_{nB}}{n_{i0}}$ with discharge voltage or due to an ingested neutral flux that is dominated by neutrals with a bulk velocity equal to the ion exhaust velocity. We can at least conclude that F_7 may also be useful to reduce the dimensionality of pressure facility effects.

In addition, in Fig. 13, F_2 does not capture the change in T^* at different voltages. At the constant cathode flow fraction between the different discharge voltages in Fig. 13, F_2 is proportional to F_1, F_6, and F_9. These nondimensional pressure parameters do not have a strong dependence on discharge voltage, so it is expected that they are not able to capture the dependence of T^* on the discharge voltage.

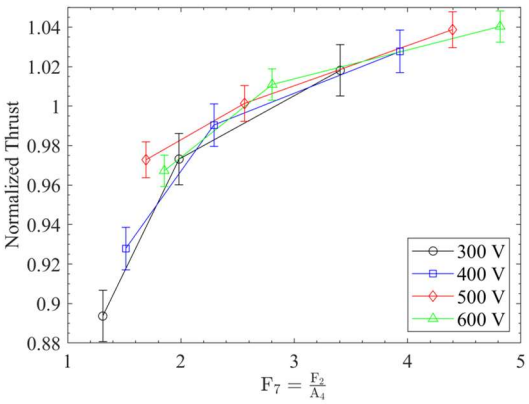

Figure 12. Normalized thrust as a function of $F_7 = \frac{F_2}{A_4}$ evaluated at $F_7^0 = 2.5$ for different discharge voltages at constant flow rate. Background pressures vary from 5 to 14 μTorr-Xe. Data adapted from Ref. 2.

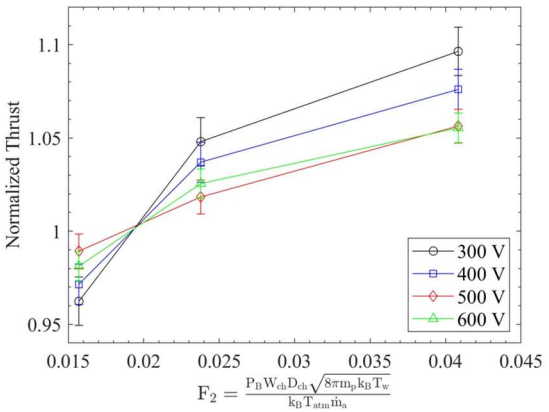

Figure 13. Normalized thrust as a function of $F_2 = \frac{P_B W_{ch} D_{ch} \sqrt{8\pi m_p k_B T_w}}{k_B T_{atm} \dot{m}_a}$ evaluated at $F_2^0 = 0.0182$ for different discharge voltages at constant flow rate. Background pressures vary from 5 to 14 μTorr-Xe. Data adapted from Ref. 2.

Next, due to measurement uncertainty, we cannot confidently conclude from Figs. 14 and 15, whether F_2 or F_9 is more important to capture the effect of the cathode flow fraction on T^*. F_9 is the only nondimensional pressure

parameter that we have defined that depends on the cathode flow fraction, so we would expect that it is able to more accurately capture the effect of the cathode flow fraction on T^*. The fact that the various curves of T^* are all within measurement uncertainty indicates that the cathode flow fraction does not strongly affect T^*, at least within the ranges of cathode flow fractions considered in Ref. 3.

This conclusion is in contrast to the conclusions in Ref. 3, which suggested that an increased cathode flow fraction reduced pressure facility effects. This contrast can be explained through the F_9 parameter. With a constant range of background pressures considered, as the cathode flow fraction increases, the range of F_9 considered decreases. Thus, conditions with a higher cathode flow fraction traverse a smaller part of the $T^*(F_9)$ curve and should correspondingly see a smaller drop in thrust for a given change in background pressure. This effect is seen in Fig. 15. However, this effect also limits the conclusions that we can make about the universality of $T^*(F_9)$ when $T^* > 1$, since the curve for the highest cathode flow fraction in Fig. 15 only has one point for which $T^* > 1$. To study the universality of $T^*(F_9)$, future pressure studies should accordingly increase the maximum background pressure for the high cathode flow fraction cases.

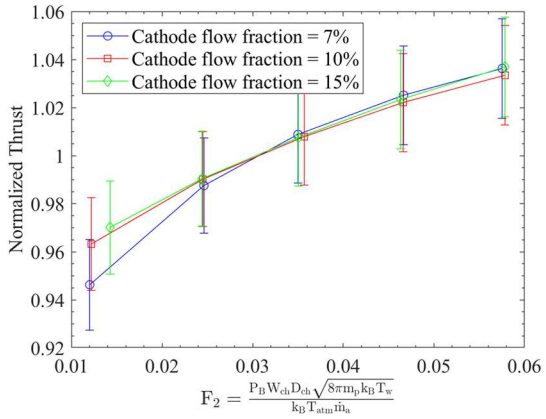

Figure 14. Normalized thrust as a function of $F_2 = \frac{P_B W_{ch} D_{ch} \sqrt{8\pi m_p k_B T_w}}{k_B T_{atm} \dot{m}_a}$ evaluated at $F_2^0 = 0.03$ for different cathode flow fractions. Background pressures vary from 5 to 20 μTorr-Xe. Data adapted from Ref. 3.

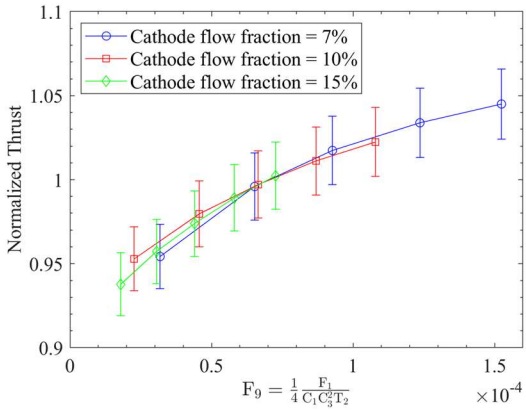

Figure 15. Normalized thrust as a function of $F_9 = \frac{1}{4} \frac{F_1}{C_1 C_3^2 T_2}$ evaluated at $F_9^0 = 7 \times 10^{-5}$ for different cathode flow fractions. Background pressures vary from 5 to 20 μTorr-Xe. Data adapted from Ref. 3.

A. Discussion

The cathode flow fraction example highlights the importance of viewing facility effects from a nondimensional perspective. While it may seem that a certain parameter reduces facility effects, it may just change the location of the experimental condition on the plot of T^*, such that the same trends would be seen when comparing thrust values in a VTF to those in space. However, if T^* depends on the discharge condition, then the discharge condition or thruster design could be manipulated to reduce facility effects.

Having presented a preliminary implementation of a nondimensional analysis of existing pressure studies, we believe that higher fidelity models of pressure facility effects should be combined with the nondimensional framework

presented here and with newly designed experiments. Even if such models do not account for charge-exchange effects or electron transport effects, we believe that, at sufficiently low pressures, nondimensional models for ingestion and cathode coupling should include all the nondimensional parameters of which T^* is a function.

Once such nondimensional parameters are defined, future experiments can be specially designed to take advantage of the nondimensional framework. The main considerations for future experiments should be the challenges outlined in Section III.D. First, to be able to compare multi-dimensional plots of T^* across multiple discharge conditions, the discharge conditions and pressure range must be carefully chosen such that all the discharge conditions share a common set of the relevant nondimensional parameters. Second, for each discharge condition, the mass flow rates should be kept constant with the different background pressures. Third, a temperature that is representative of T_w should be measured to distinguish between F_1 and F_2. Lastly, experiments should be performed to determine whether the mechanism with which the background pressure is increased changes the ratio of the ingested flux to the thermal flux. Furthermore, we note that this nondimensional framework can be easily extended to analyze the pressure dependence of the discharge current and thruster lifetime.

In addition, there is a clear need to access the lower parts of the T^* curve. However, doing so is not necessarily a matter of operating at lower background pressures. $\frac{P_B}{\dot{m}_a}$ is inversely proportional to the effective facility pumping speed, so lower flow rates should not inherently result in smaller nondimensional pressure parameters that are relevant to T^*. Facilities with higher pumping speeds are clearly one solution to reaching lower parts of the T^* curve. However, as shown in Figs. 11, 12, and 15, lower anode flow rates, voltages, and cathode flow fractions could also be used to reach lower parts of the T^* curve.

Lastly, regarding the testing of high-power HETs, it is typically considered that newer facilities with higher pumping speeds are needed to flight qualify them. High pumping speeds will allow operating at lower values of $\frac{P_B}{\dot{m}_a}$ and of background pressures, corresponding to lower values of F_1, F_2, F_3, and F_8, which is clearly beneficial. However, in current state-of-the-art vacuum chambers, F_1 and F_2 should not change much with discharge power, as they are proportional to $\frac{P_B}{\dot{m}_a}$. So, if the current vacuum chambers are adequate for flight qualification of medium-power HETs, they should be able to achieve adequate values of F_1 and F_2 for high-power HETs. The challenge for testing high-power HETs in current facilities must then be due to high values of F_3, F_8, and F_9, which are proportional to P_B and not to $\frac{P_B}{\dot{m}_a}$. In fact, at sufficiently high background pressures, a HET may no longer run in its nominal mode due to high values of F_3, F_8, and F_9.

However, a medium-power HET that is exactly similar to a high-power HET would operate at lower background pressures than the corresponding high-power HET. Therefore, operating a medium-power HET in current vacuum chambers would be exactly similar to a high-power HET operating at values of F_1, F_2, F_3, F_8, and F_{10} that are adequate for flight qualification. If a high-power HET is designed to be exactly similar to a medium-power HET that is already flight qualified, then the extensive tests that are required for flight qualification of a new design may not be necessary. Instead, it could just go through acceptance testing that is required for new thruster units of the same design.

Therefore, the required pumping speed of new facilities for the purpose of testing high-power HET should be based on the requirements of acceptance testing. Such a requirement should be based on the ability during high-power operation to achieve background pressures low enough such that F_3, F_8, and F_{10} have a negligible contribution to T^* (and normalized discharge current too). This is because even if two thrusters are exactly similar but operate at different flow rates, their corresponding T^* functions can only be the same in regions where F_3, F_8, and F_{10} are negligible. This

is since F_3, F_8, and F_{10} are proportional P_B, while F_1 and F_2 are proportional to $\frac{P_B}{\dot{m}_a}$. So, at different flow rates, F_1, F_2, F_3, F_8, and F_{10} cannot all be equal. As a result, experiments should be conducted to identify at which pressure F_3, F_8, and F_{10} become negligible, as this pressure would define the required pumping speed for an acceptance test for a thruster at a given flow rate.

For the acceptance test, the medium-power HET would also need to be tested in the high-pumping speed facility, such that the medium-power HET is characterized with the same pumping speed as the high-power HET. Then, the high-power HET can be tested at the same values of F_1 as the medium-power HET, such that both thrusters were operated at the same point on the T^* function, since T^* is defined by F_1 when F_3, F_8, and F_{10} are negligible and when the two thrusters are exactly similar. So, if the high-power HET is correctly manufactured and the above conditions are met, then its thrust should compare to the thrust of the medium-power HET according to the scaling law.

VI. Conclusion

The nondimensional framework has been used to propose new paths for improving our understanding of HET scaling and of pressure facility effects. The presented HET similarity seems to be most useful for extending HET performance to different propellants and possibly to lower powers. We have also found that the only way for an exact similarity law to exist is if wall effects are negligible and that at a sufficiently high current density, wall effects should become negligible for annular HETs of a given channel aspect ratio. Regarding facility effects, we have presented a nondimensional framework to analyze pressure studies and have found that the framework can be used to reduce the dimensionality of pressure facility effects at different discharge conditions.

In terms of future work on HET scaling, there are a few possible directions. First, our generalized similarity laws can be combined with better models for how the electron temperature, electron density, and axial electron drift velocity change with discharge condition to increase the accuracy of how V_d, B_{r0}, and $\dot{m}_a$ should change with discharge condition and how L_{ch} should change with propellant. Second, experiments should be carried out to test the presented similarity laws; the most straightforward one to test is the similarity laws between different propellants on the same thruster, as this does not require designing a new HET. Third, two HETs should be designed based on the similarity of Eq. 16 to determine what current density is required to achieve similarity between the thrusters. Fourth, existing HET efficiency data can be analyzed with a nondimensional framework to try to find the minimum set of nondimensional parameters that describe efficiency trends over a wide range of conditions; identifying the nondimensional parameters most relevant to HET performance could result in alternative similarity laws. Lastly, we believe that efforts should be made to increase the efficiency and lifetime of wall-less HETs, as they would be able to achieve exact similarity at any power level while maintaining constant thrust density and current density.

Development of efficient HET designs that can be scaled with exact similarity should reduce the pumping speed requirements for qualification of high-power HETs. Once such an efficient design is developed, experiments can be designed to establish the criterion for the background pressure at which the pressure facility effects are similar between a medium-power and high-power HET. Before such an efficient design is developed, the nondimensional framework can still be leveraged to experimentally determine a nondimensional correction for thrust as a function of pressure that should be applicable to a wide variety of discharge conditions. As a result, the nondimensional framework can be of use for scaling and facility effect work in the near future and should continue to be of use when HETs at new power levels are developed.

Appendix

The thermal model described below is adapted from Ref. 54. The characteristic thruster wall temperature is obtained from the power balance of the characteristic power deposited into the channel wall, P_{w0}, and into the anode, P_{w0}, from the plasma against the characteristic net power radiated from the thruster, Q_{net},

$$P_{w0} + P_{a0} = Q_{net}, \tag{A-1}$$

where

$$Q_{net} = \sigma_{SB}\varepsilon_R A_R F(T_w^4 - T_{atm}^4), \tag{A-2}$$

$$P_{w0} = eA_w\Gamma_{iw0}\left(2T_{ew,0} + \frac{1}{2}T_{ew,0} + \Phi_s\right), \tag{A-3}$$

$$P_{a0} = 2T_{ea,0}I_{d,0}. \tag{A-4}$$

Φ_s is the potential drop across the sheath at the channel wall, $\frac{1}{2}T_{ew,0}$ is the presheath ion energy, $T_{ea,0}$ is the characteristic electron temperature at the anode, and $I_{d,0}$ is the characteristic discharge current. Using $T_{ea,0} = \frac{V_d}{100}$, $I_{d,0} = \frac{e\dot{m}_a}{m_p}$, $\Phi_s = T_{ew,0}\ln\left((1-\sigma_{SEE})\sqrt{\frac{m_p}{2\pi m_e}}\right)$, and $A_R = \pi\left(L_{ch}(W_{ch}+D_{ch}) + \frac{1}{2}(W_{ch}+D_{ch})^2\right)$ along with the previous definitions for characteristic plasma properties, we find that

$$T_w^4 = T_{atm}^4 + \frac{eV_d\dot{m}_a}{m_p\sigma_{SB}\varepsilon_R F}\frac{1}{\pi\left(L_{ch}(W_{ch}+D_{ch})+\frac{1}{2}(W_{ch}+D_{ch})^2\right)}\left(\frac{1}{50} + \frac{T_1}{\pi 20\sqrt{5}}\left[\frac{5}{2} + \ln\left(T_3\sqrt{\frac{1}{2\pi P_1}}\right)\right]\right). \tag{A-5}$$

For all applications of this model, we will assume ε_R = 0.3 and F = 1.

Acknowledgements

Funding for this work was provided by NASA in part through the Joint Advanced Propulsion Institute (JANUS), a NASA Space Technology Research Institute, under grant number 80NSSC21K1118, as well as in part through NASA Space Technology Graduate Research Opportunity grants 80NSSC23K1217 and 80NSSC20K1224.

References

[1] Snyder JS, Lenguito G, Frieman JD et al. Effects of background pressure on SPT-140 Hall thruster performance. J Propuls Power 36(5). 2020. https://doi.org/10.2514/1.B37702

[2] Walker MLR. Effects of facility backpressure on the performance and plume of a Hall thruster. PhD thesis, University of Michigan. 2005.

[3] Cusson SE, Byrne M, Jorns B et al. Investigation into the use of cathode flow fraction to mitigate pressure-related facility effects on a magnetically shielded Hall thruster. In: Proceedings of the Propulsion and Energy Forum (AIAA Paper 2019-4077). 2019.

[4] Hofer RR, Anderson JR. Finite pressure effects in magnetically shielded Hall thrusters. In: Proceedings of the 50th Joint Propulsion Conference (AIAA Paper 2014-3709). 2014.

[5] Diamant KD, Liang R, Corey RL. The effect of background pressure on SPT-100 Hall thruster performance. In: Proceedings of the 50th Joint Propulsion Conference (AIAA Paper 2014-3710). 2014.

[6] Kamhawi H, Huang W, Haag T et al. Performance, facility pressure effects, and stability characterization tests of NASA's Hall effect rocket with magnetic shielding thruster. In: Proceedings of the 52nd Joint Propulsion Conference (AIAA Paper 2016-4826). 2016.

[7] Smirnov A, Raitses Y, Fisch NJ. Experimental and theoretical studies of cylindrical Hall thrusters. Phys Plasmas 14: 057106. 2007. https://doi.org/10.1063/1.2718522

[8] Mazouffre S, Tsikata S, Vaudolon J. Development and experimental characterization of a wall-less Hall thruster. J Appl Phys 116: 243302. 2014. https://doi.org/10.1063/1.4904965

[9] Karadag B, Cho S, Funaki I. Thrust performance, propellant utilization, and thruster erosion of an external discharge plasma thruster. J Appl Phys 123: 153302. 2018. https://doi.org/10.1063/1.5023829

[10] Simmonds J, Raitses Y. Ion acceleration in a wall-less Hall thruster. J Appl Phys 130: 093302. 2021. https://doi.org/10.1063/5.0062607

[11] Hall SJ, Jorns BA, Cusson SE et al. Performance and high-speed characterization of a 100-kW nest Hall thruster. J Propuls Power 38(1). 2021. https://doi.org/10.2514/1.B38080

[12] Szabo J, Pote B, Paintal S et al. Performance evaluation of an iodine-vapor Hall thruster. J Propuls Power 28(4). 2012. https://doi.org/10.2514/1.B34291

[13] Szabo J, Robin M, Hruby V. Bismuth vapor Hall effect thruster performance and plume experiments. In: Proceedings of the 35th International Electric Propulsion Conference (IEPC Paper 2017-25). 2017.

[14] Munro-O'Brien TF, Ryan CN. Performance of a low power Hall effect thruster with several gaseous propellants. Acta Astronaut 206: 257-273. 2023. https://doi.org/10.1016/j.actaastro.2023.01.033

[15] Tirila V-G, Demaire A, Ryan CN. Review of alternative propellants in Hall thrusters. Acta Astronaut 212: 284-306. 2023. https://doi.org/10.1016/j.actaastro.2023.07.047

[16] Morozov AI, Savelyev VV. Fundamentals of Stationary Plasma Thruster Theory. In: Reviews of Plasma Physics. Springer. pp 203-391. 2000. https://doi.org/10.1007/978-1-4615-4309-1_2

[17] Khayms V, Martinez-Sanchez M. Design of a miniaturized Hall thruster for microsatellites. In: Proceedings of the 32nd Joint Propulsion Conference (AIAA Paper 96-3291). 1996.

[18] Ashkenazy J, Raitses Y, Appelbaum G. Low power scaling of Hall thrusters. In: Proceedings of the 2nd European Spacecraft Propulsion Conference. 1997.

[19] Hruby V, Monheiser J, Pote B et al. Development of low power Hall thrusters. In: Proceedings of the 30th Plasmadynamics and Lasers Conference (AIAA Paper 99-3534). 1999.

[20] Dannenmayer K, Mazouffre S. Elementary Scaling Relations for Hall effect Thrusters. J Propuls Power 27(1). 2011. https://doi.org/10.2514/1.48382

[21] Shagayda AA, Gorshkov OA. Hall-thruster scaling laws. J Propuls Power 29(2). 2013. https://doi.org/10.2514/1.B34650

[22] Fu Y, Wang H, Wang X. Similarity theory and scaling laws for low-temperature plasma discharges: a comprehensive review. Rev Mod Plasma Phys 7, 10. 2023. https://doi.org/10.1007/s41614-022-00112-1

[23] Zhao Z, Wang Z, Duan Z, Fu Y. Dynamic similarity of streamer propagation in geometrically similar combined air gaps. IEEE Trans Dielectr Electr Insul 32(2): 1017-1026. 2025. https://doi.org/10.1109/TDEI.2024.3457594

[24] Yang D, Verboncoeur JP, Fu Y. Demonstration of similarity laws and scaling networks for radio-frequency plasmas. Phys Rev Lett 134, 045301. 2025. https://doi.org/10.1103/PhysRevLett.134.045301

[25] Cusson S. Impact of neutral density on the operation of high-power magnetically shielded Hall thrusters. PhD thesis, University of Michigan. 2019.

[26] Tighe WG, Spektor R, Diamant KD, Kamhawi H. Effects of background pressure on the NASA 173M Hall current thruster performance. Proceedings of the 34th International Electric Propulsion Conference (IEPC Paper 2015-152). 2015.

[27] Piragino A, Faraji F, Reza M, Ferrato E, Praino A, Andreussi T. Background pressure effects on the performance of a 20 kW magnetically shielded Hall thruster operating in various configurations. Aerospace 8, 69. 2021. https://doi.org/10.3390/aerospace8030069

[28] Hirakawa M, Arakawa Y. Particle simulation of plasma phenomena in Hall thrusters. In: Proceedings of the 24th International Electric Propulsion Conference (IEPC Paper 95-164). 1995.

[29] Donko Z. Apparent second-electron emission coefficient and the voltage-current characteristics of argon glow discharges. Phys Rev E 64, 026401. 2001. https://doi.org/10.1103/PhysRevE.64.026401

[30] Hirabayashi K, Hoshino M, Amano T. A new framework for magnetohydrodynamic simulations with anisotropic pressure. J Comput Phys 327 : 851-872. 2016. https://doi.org/10.1016/j.jcp.2016.09.064

[31] Cavalier J, Lemoine N, Bonhomme G et al. Hall thruster plasma fluctuations identified as the ExB electron instability, Modeling and fitting on experimental data. Phys Plasmas 20: 082107. 2013. https://doi.org/10.1063/1.4817743

[32] Villafana W, Cuenot B, Vermorel O. 3D particle-in-cell study of the electron drift instability in a Hall thruster using unstructured grids. Phys Plasmas 30: 033503. 2023. https://doi.org/10.1063/5.0133963

[33] Barral S, Makowski K, Peradzynski Z et al. Wall material effects in stationary plasma thrusters. II. Near-wall and in-wall conductivity. Phys Plasmas 10: 4137-4152. 2003. https://doi.org/10.1063/1.1611881

[34] Hara K, Sekerak MJ, Boyd ID et al. Mode transition of a Hall thruster discharge plasma. J Appl Phys 115: 203304. 2014. https://doi.org/10.1063/1.4879896

[35] Dominguez-Vazquez A, Taccogna F, Ahedo E. Particle modeling of radial electron dynamics in a controlled discharge of a Hall thruster. Plasma Sources Sci Technol 27(6): 064006. 2018. https://doi.org/10.1088/1361-6595/aac968

[36] Poli D, Fajardo P, Ahedo E. A non-neutral 1D fluid model of Hall thruster discharges: full electron inertia and anode sheath reversal. Plasma Sources Sci Technol 33(7): 075014. 2024. https://doi.org/10.1088/1361-6595/ad6500

[37] Goebel DM, Katz I, Mikellides IG. Fundamentals of Electric Propulsion. Wiley. 2023.

[38] Achenbach C, Muller A, Salzborn E et al. Single ionization of multiply charged xenon ions by electron impact. J Phys B 17(7): 1405. 1984. https://doi.org/10.1088/0022-3700/17/7/023

[39] Goebel DM, Hofer RR, Mikellides IG et al. Conducting wall Hall thrusters. IEEE Trans Plasma Sci 43(1): 118-126. 2015. https://doi.org/10.1109/TPS.2014.2321110

[40] Grimaud L, Mazouffre S. Conducting wall Hall thrusters in magnetic shielding and standard configurations. J Appl Phys 122: 033305. 2017. https://doi.org/10.1063/1.4995285

[41] Ahedo E, Gallardo JM, Martinez-Sanchez M. Model of the plasma discharge in a Hall thruster with heat conduction. Phys Plasmas 9: 4061-4070. 2002. https://doi.org/10.1063/1.1499496

[42] Hara K, Tsikata S. Cross-field electron diffusion due to the coupling of drift-driven microinstabilities. Phys Rev E 102: 023202. 2020. https://doi.org/10.1103/PhysRevE.102.023202

[43] Jovel DR. Impedance characterization of a Hall effect thruster discharge in a ground-based vacuum test facility. PhD thesis, Georgia Institute of Technology. 2023.

[44] Spektor R. Analytical pumping speed models for electric propulsion vacuum facilities. J Propuls Power 37(3). 2020. https://doi.org/10.2514/1.B37998

[45] Brown DL, Walker MLR, Szabo J, et al. Recommended practice for use of Faraday probes in electric propulsion testing. J Propuls Power 33(3). 2017. https://doi.org/10.2514/1.B35696

[46] Frieman JD, Liu TM, Walker MLR. Background flow model of Hall thruster neutral ingestion. J Propuls Power. 2017 33(5). https://doi.org/10.2514/1.B36269

[47] Mikellides IG, Lopez Ortega A, Chaplin VH, et al. Facility pressure effects on a Hall thruster with an external cathode, II: theoretical model of the thrust and the significance of azimuthal symmetries in the cathode plasma. Plasma Sources Sci Technol 29(3): 035010. 2020. https://doi.org/10.1088/1361-6595/ab6c7f

[48] Cusson SE, Jorns B, Gallimore A. Simple model for cathode coupling voltage versus background pressure in a Hall thruster. In: Proceedings of the 53rd Joint Propulsion Conference (AIAA Paper 2017-4889). 2017.

[49] Crofton MW, Dale ET, Thuppul A. Electric thruster ingestion and background propellant density measurements. In: Proceedings of the 38th International Electric Propulsion Conference (IEPC Paper 2024-367). 2024.

[50] Su LL, Roberts PJ, Gill TM et al. High-current density performance of a magnetically shielded Hall thruster. J Propuls Power 40(5). 2024. https://doi.org/10.2514/1.B39324

[51] Marianacci A, Mazouffre S. Supervised machine learning-based Hall thruster scaling. J Electr Propuls 3: 14. 2014. https://doi.org/10.1007/s44205-024-00077-y

[52] Giammarinaro G, Marconcini F, Becatti G. A scaling methodology for high-power magnetically shielded Hall thruster. J Electr Propuls 2: 17. 2023. https://doi.org/10.1007/s44205-023-00049-8

[53] Rejoub R, Lindsay BG, Stebbings RF. Determination of the absolute partial and total cross sections for electron-impact ionization of the rare gases. Phys Rev A 65: 042713. 2002. https://doi.org/10.1103/PhysRevA.65.042713

[54] Conversano RW, Goebel DM, Hofer RR, Matlock TS, Wirz RE. Development and initial testing of a magnetically shielded miniature Hall thruster. IEEE Trans Plasma Sci 43(1): 103-117. 2015. https://doi.org/10.1109/TPS.2014.2321107